

## Article

# Structural Engineering of $\pi$ -Linker Aromaticity in Anthanthrene-Based Dyes with D- $\pi$ -A Configuration: DFT Investigation to Enhance Charge Transfer in DSSCs

Nuha Wazzan

Chemistry Department, Faculty of Science, King Abdulaziz University, P.O. Box 42805, Jeddah 21589, Saudi Arabia; nwazzan@kau.edu.sa

**Abstract:** The development of efficient dyes for photon harvesting in dye-sensitized solar cells (DSSCs) is a critical area of research with the potential to enhance renewable energy technologies. This manuscript presents a novel approach to engineering dye structures (abbreviated as D2 dye features, an anthanthrene core with a resonance energy of  $E_R = 694$  kJ/mol and a reported power conversion efficiency ( $\eta$ ) of 5.27%) by systematically replacing an anthanthrene core with various aromatic cores, aiming to understand the influence of resonance energy on molecular performance. By designing seven new dyes with resonance energies ranging from 255 to 529 kJ/mol, we conducted in-depth computational studies using Density Functional Theory (DFT) and Time-Dependent Density Functional Theory (TDDFT) to explore the effects of  $\pi$ -aromatic linkers on their electronic properties. Our findings reveal key insights into intermolecular charge-transfer (ICT) mechanisms and how they relate to the resonance energy of dye cores, highlighting the significance of balanced charge mobilities in optimizing optoelectronic characteristics, as shown by the D9 dye with a naphthacene core.

**Keywords:** anthanthrene-based dyes; resonance energies; DFT calculations; adsorption energies; intramolecular charge transfer (ICT)



Academic Editors: Chenyu Wu, Zhongkai Yi, Chenhui Lin and Xi Chen

Received: 21 December 2024

Revised: 8 January 2025

Accepted: 13 January 2025

Published: 5 February 2025

**Citation:** Wazzan, N. Structural Engineering of  $\pi$ -Linker Aromaticity in Anthanthrene-Based Dyes with D- $\pi$ -A Configuration: DFT Investigation to Enhance Charge Transfer in DSSCs. *Processes* **2025**, *13*, 418. <https://doi.org/10.3390/pr13020418>

**Copyright:** © 2025 by the author. Licensee MDPI, Basel, Switzerland. This article is an open access article distributed under the terms and conditions of the Creative Commons Attribution (CC BY) license (<https://creativecommons.org/licenses/by/4.0/>).

## 1. Introduction

Technologies based on solar energy have remarkably developed during the last few decades. This is because of global concerns regarding the cost and availability of fossil fuels and the harmful effects on the worldwide climate due to the use of fossil fuels [1]. Regarding energy resources, the sun is considered the largest renewable source of energy. The sun provides the earth with 173,000 TW of energy per year [2], which means that one hour of the sun's energy is more than what the human population consumes in one year. For 30 years, Grätzel and O'Regan 1991 developed solar cells with a new design known as Grätzel's cells or dye-sensitized solar cells (DSSCs) [3]. A DSSC joins nanoparticles and molecular systems in a device like when a photosynthesis process takes place, and this device can convert sunlight into reliable, low-cost, and renewable energy [4]. In a DSSC device, the photosensitizer/dye (the light harvester) plays a crucial role. The dye used for this application must meet the following criteria: (i) captures visible/near-infrared light (Vis/NIR); (ii) absorbs light intensely, i.e., its molar absorption coefficient should be high; (iii) the appropriate alignment of its frontier molecular orbitals (FMOs), i.e., the energy of its LUMO (lowest unoccupied molecular orbital), is positioned above the semiconductor's conduction band (CB) edge, and its energy of HOMO (highest occupied molecular orbital) is positioned lower than the redox shuttle for the effective regeneration of it; and (iv) a

rendering of its aggregation on the  $\text{TiO}_2$  surface is required [5]. A dye based on Ruthenium could be used [6,7]. However, Ruthenium-based dyes are not available in nature, usually come with high production costs, and are toxic. Among the other types of dyes are those based on porphyrins [8]. Porphyrin-based dyes have the advantage of good absorption in the Vis region [5]. Lastly, dyes can be metal-free (MF) photosensitizers. MF-based dyes are promising candidates. They are low in production cost, are associated with high molar absorption coefficients, and are environment-friendly [9]. Most MF dyes are push–pull configured, which means an electron-donor unit (D) is connected to an electron-acceptor unit by a core forming a  $\pi$ -bridge. Since the choice of the  $\pi$ -bridge core is a vital factor in the potential performance of DSSC devices, researchers have investigated, experimentally and theoretically, the effects of various  $\pi$ -linker cores on the optoelectronic characteristics of the resultant dyes [10–13]. Such  $\pi$ -bridge cores are thiophene cores [10], azo cores [11], and cyanovinyl cores [12]. It is uncommon to find experimental and theoretical studies of dyes based on anthanthrene cores in the literature [14–16]. These dyes possess unique structural and electronic properties that may lead to improved performance in DSSCs and other optoelectronic applications.

Our study aims to explore these properties in the context of dye–semiconductor interactions. In materials science, naphtho[7,8,1,2,3-nopqr]tetraphene (anthanthrene) represents a promising building block. A series of anthanthrene-based photosensitizers have been investigated in DSSCs experimentally by Geng et al. [15]. Also, Wazzan [14] tried to interpret this work by detailed DFT calculations. The four synthesized dyes have a donor unit (triphenylamine); an anthanthrene unit, which serves as a conjugated  $\pi$ -linker; and one or two cyanoacrylic acid groups, which substitute 3-ethylheptane or nonane alkyl chains into the anthanthrene core and serve as anchoring groups. The performance of DSSC devices has been evaluated based on how many anchoring groups are present and the type of alkyl substitution used. Among the four investigated dyes, D2, (E)-2-cyano-3-(5-(10-(4-(di-p-tolylamino)phenyl)-6,12-bis(octyloxy)naphtho[7,8,1,2,3-nopqr]tetraphen-4-yl)thiophen-2-yl)acrylic acid, a dye-based device, exhibits the largest short-circuit current ( $J_{sc}$ ), which equals  $10.4 \text{ mA cm}^{-2}$ , offers a top overall power conversion efficiency ( $\eta$ ) of 5.27% (the fill factor (FF) equals 0.73 and the open-circuit voltage ( $V_{oc}$ ) equals 690 mV).

In an effort by the group of Venkatraman et al. [17], various dyes have been designed in which the triphenylamine group acts as the donor unit, and cyanoacrylic acid unit acts as the anchoring group, and a number of aromatic rings with different resonance energies (benzene (36 kcal/mol), pyridine (32 kcal/mol), furan (16 kcal/mol), pyrrole (21 kcal/mol), and thiophene (29 kcal/mol)), act as  $\pi$ -linkers. The aromaticity of  $\pi$ -linkers on the configurational, electro-optical, photovoltaic, and charge-transfer properties have been investigated and analyzed. A conclusion was drawn in such a way that a complex relationship has been found to exist between aromaticity and photovoltaic properties. As described by Pino-Rios et al. [18], porphyrin cores have been modified to gain improved behavior as light harvesters in the UV, Vis, and NIR regions. A moiety of oxazolone has replaced the imine ring, resulting in redshifts and an enhanced Q-band intensity with respect to reference compounds. Moreover, aromaticity was explained using delocalization and magnetic criteria. Descriptors of aromaticity and Q bands show a qualitative relationship, and thus, as concluded, this has potential in the rational design of photosensitizers. In a theoretical investigation by Obasuyi et al. [9], using functional MN12SX with a 6-311+G(d,p) basis set, two series of anthocyanidin and betalain families were studied. Aromaticity, the open-circuit voltage ( $V_{oc}$ ), the rate constant of the injection ( $\Delta G_{inj}$ ), and the rate constant of the dye regeneration ( $\Delta G_{reg}$ ) values were found to play important roles in determining which dye is most efficient. In another theoretical effort by Borges-Martínez

et al. [5], BODIPY and oxasmaragdyrin photosensitizers were studied using 11 bridging functional groups on their aromatic, charge transport, and photophysical properties. At the GIAO/B3LYP/6-311G(d,p) level, the aromaticity index, NICS(0), is calculated at the macrocycle center-ring critical point, and all these systems can be classified as aromatic (between  $-10.7$  and  $-12.4$  ppm).

Historically, one of the first energy-based quantities used to quantify the degree of aromaticity is the resonance energy ( $E_R$ ). Based on a comparison of the energy values of the localized Lewis structure and the delocalized “real” compound, the  $E_R$  value is determined. Electronic configurations representing a localized Lewis structure can be calculated and compared using a restraint-free calculation that allows for full delocalization. Aromaticity increases as this difference rises [19]:

$$E_R = E_{\text{del}} - E_{\text{Lewis}} \quad (1)$$

where  $E_{\text{del}}$  is the electronic energy of the fully delocalized structure, and  $E_{\text{Lewis}}$  is the electronic energy of the most representative Lewis structure.

To compensate for the spectral engineering of DSSCs for new applications such as greenhouse-oriented applications, developments of DSSCs that employ newly designed dyes have been considered a lot in the literature [20]. Greenhouses typically utilize sunlight, but their spectral composition can vary based on the time of day and season. The sunlight that reaches plants in a greenhouse includes a range of wavelengths—primarily, visible light, with some near-infrared (NIR) and ultraviolet (UV) components. The first step in spectral engineering involves designing dyes that have specific absorption characteristics that can complement or optimize the light available in a greenhouse.

This study addresses a significant challenge in the field of DSSCs—the need for improved light-to-current efficiency through the strategic optimization of dye structures. As mentioned in the above refs. [5,9,17,18], current research highlights a promising correlation between aromaticity and photovoltaic performance, but there remains a gap in understanding how different resonance energies within dye molecules can influence their effectiveness in energy conversion. By focusing on the superior capabilities of the D2 dye, as substantiated in ref. [15], this work presents novel dyes designed by substituting the anthanthrene linker with various aromatic rings, each characterized by distinct resonance energies. This innovative approach aims not only to enhance optical and photovoltaic properties but also to provide valuable insights into the structure–property relationships that govern the performance of DSSCs. The significance of this study lies in its potential to bridge existing knowledge gaps, and it offers a systematic investigation into how modifications at the molecular level can lead to enhanced energy conversion efficiencies.

The molecular structures of the seven designed dyes are illustrated in Figure 1. Abbreviations and IUPAC names of the designed dyes are as follows: D5: (E)-2-cyano-3-(5-(6-(4-(diphenylamino)phenyl)-4,8-bis(octyloxy)anthracen-2-yl)thiophen-2-yl)acrylic acid; D6: (E)-2-cyano-3-(5-(6-(4-(diphenylamino)phenyl)-3,8-bis(octyloxy)phenanthren-1-yl)thiophen-2-yl)acrylic acid; D7: (E)-2-cyano-3-(5-(6-(4-(diphenylamino)phenyl)-3,8-bis(octyloxy)phenanthren-1-yl)thiophen-2-yl)acrylic acid; D8: (E)-2-cyano-3-(5-(8-(4-(diphenylamino)phenyl)-1,6-bis(octyloxy)pyren-4-yl)thiophen-2-yl)acrylic acid; D9: (E)-2-cyano-3-(5-(8-(4-(diphenylamino)phenyl)-4,10-bis(octyloxy)tetracen-2-yl)thiophen-2-yl)acrylic acid; D10: (E)-2-cyano-3-(5-(1-(4-(diphenylamino)phenyl)-3,9-bis(octyloxy)chrysen-6-yl)thiophen-2-yl)acrylic acid; and D11: (E)-2-cyano-3-(5-(9-(4-(diphenylamino)phenyl)-5,11-bis(octyloxy)perylene-3-yl)thiophen-2-yl)acrylic acid. In this work, by critically analyzing both the well-performing D2 dye and its seven newly designed derivatives, we aim to furnish the field with a deeper understanding of how structural variations impact the performance of photosensitizers in DSSCs. Ultimately, our findings could pave the way for the development of

more efficient solar energy materials, contributing to advancements in renewable energy technologies and addressing global energy challenges. The synthesis procedure of the D2 dye, as described in ref. [15], along with the suggested synthesis procedures for the newly designed dyes are illustrated in Figure 2.

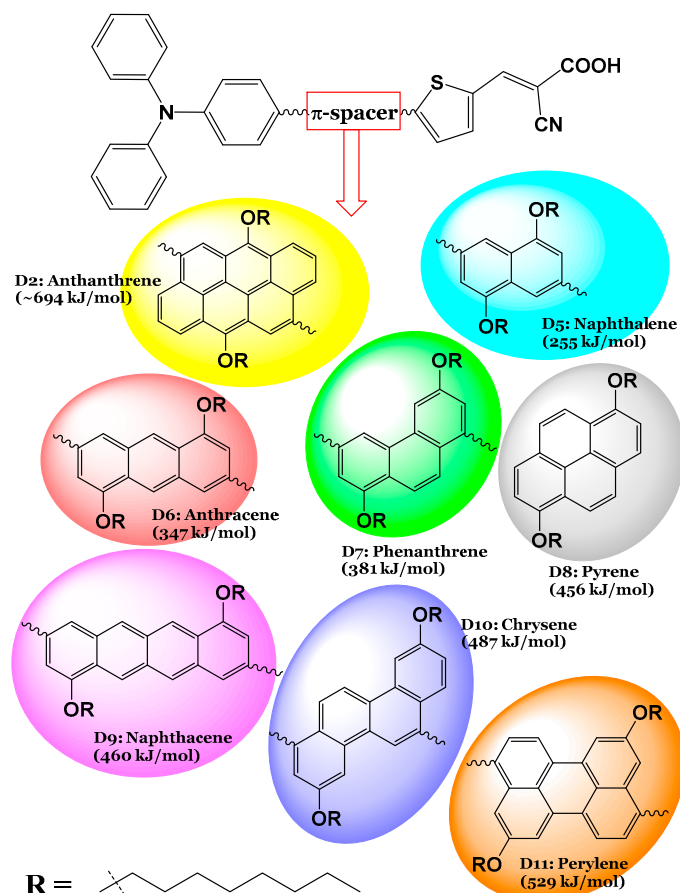


**Figure 1.** The seven designed dyes (D5 to D11) from the most efficient D2 dye (indicated too) [15], obtained by replacing the  $\pi$ -spacer unit in D2 (anthanthrene) by aromatic rings with different resonance energies (in kJ/mol).

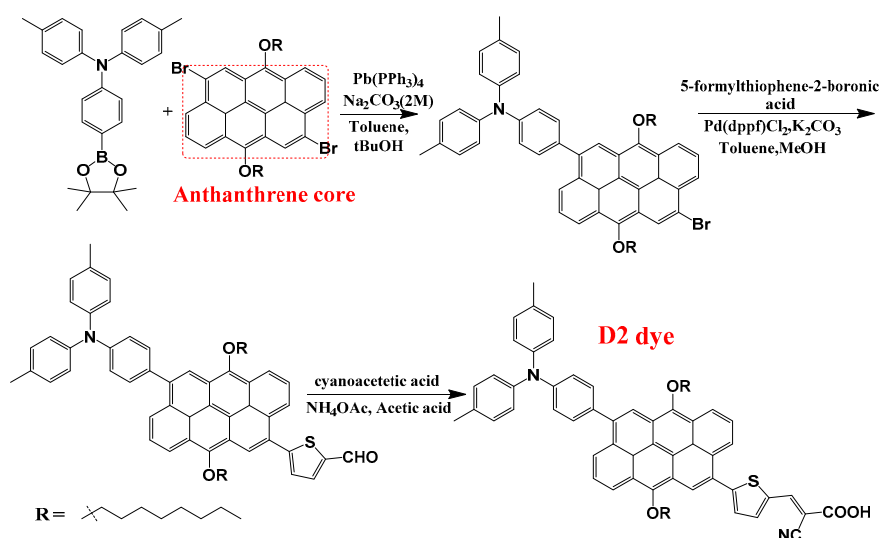


**Figure 2.** The synthesis procedure of D2, as adopted from ref. [15]. The designed dyes, D5 to D11, can be synthesized by replacing the anthanthrene core with naphthalene, anthracene, phenanthrene, pyrene, naphthacene, chrysene, and perylene cores, respectively.



## 2. Methods

Regarding DFT theory, a series of dyes based on anthanthrene were optimized with no structural constraints imposed on the optimization. An M06-2x hybrid functional from the Truhlar group was used for DFT calculations [21], using the standard basis set of 6-31+G(d,p) [22,23]. The M06-2x functional was selected due to its proven reliability and accuracy in describing non-covalent interactions, which are particularly relevant for the system under investigation. Numerous studies have highlighted its capacity to effectively handle dispersion interactions, making it suitable for systems involving dye–semiconductor interactions [24]. Furthermore, the M06-2x functional has shown favorable performance in comparison to other functionals, such as B3LYP and PBE0 [25], particularly in terms of predicting reaction energies and geometries in similar material systems [26,27]. The adopted basis set (6-31+G(d,p)) offers a balanced trade-off between computational efficiency and the accuracy of electronic structure calculations. 6-31+G(d,p) is a double  $\zeta$  basis set with one diffuse function and two polarizable functions. Since the experimental testing of the reference dye (D2) was carried out in a THF solvent, the Conductor-like Polarizable Continuum Model (CPCM) was utilized to replicate the appearance of this solvent (THF,  $\epsilon = 7.58$ ). The choice of the CPCM model is supported by various studies in the literature that investigate dye behavior in DSSC applications. It has shown a good ability to describe the interactions that influence photovoltaic performance [15,28,29]. A simulation of dye adsorption on the TiO<sub>2</sub> surface has also been conducted. Considering the cost of computation and the reliability of the system, the cluster (TiO<sub>2</sub>)<sub>6</sub> was selected to model anatase TiO<sub>2</sub>. Anatase (TiO<sub>2</sub>)<sub>6</sub> has an optimal cluster size in terms of computational cost/efficiency negotiation to simulate the electronic and optical properties of the complex system [17,30]. Hydrogenated TiO<sub>2</sub> clusters are more stable than dehydrogenated ones, as previously demonstrated [31], so the (TiO<sub>2</sub>)<sub>6</sub>H<sub>3</sub> cluster was used. No structural constraints were applied to dye complexation geometries with TiO<sub>2</sub>, using 6-31+G(d,p) for C, O, N, S, and H. In addition, the Los Alamos National Laboratory DZ quality and the overall combination of ECP and valence basis sets (LANL2DZ) for Ti atoms were used [32]. With only real frequencies, all optimized geometries reach a minimum. Typically, exchange functionals have too-short non-coulomb parts that die off too quickly and become very inaccurate with distance. Thus, they cannot be used to model electron excitations in high orbitals. TDDFT with a coulomb-attenuating functional (CAM-B3LYP) and the same basis set has been used to calculate the absorption of 12 excited states and emission to 3 excited state transitions using the optimal geometry in the ground state [33]. The Gaussian 09 software suite was used to perform all calculations [34]. Visualizations of molecular structures were performed by using GaussView (version 5.0.8) [35]. The molecular electrostatic potential maps (MESP) were drawn using the Avogadro package [36]. Finally, the comprehensive equations employed for estimating various parameters, along with their respective references, are presented in the computational details section of the Supplementary Data (SD).

## 3. Results and Discussion

Based on the experimental results of [15] and fully supported and interpreted by the theoretical calculations of the present author [14], the D2 dye performed better than the other three dyes tested. The D2 dye's configuration was modified by replacing the  $\pi$ -spacer (Naphtho[7,8,1,2,3-nopqr]tetraphene) with aromatic rings of smaller and different resonance energies, and seven dyes were designed as a result, see Figure 1. Therefore, the eight investigated dyes consist of a donor group (triphenylamine unit (TPA)) and an anchoring group (a cyanoacrylic acid unit) attached at the 6,12 positions to a thiophene unit (TPH) and are substituted with two nonane alkyl chains (ALKY1/ALKY2) attached

to different aromatic cores. The resonance energies ( $E_R$ ) of the designed dyes and the D2 dye decrease in the following order: D2 (anthanthrene;  $E_R = \sim 694$  kJ/mol) > D11 (perylene;  $E_R = 529$  kJ/mol) > D10 (chrysene;  $E_R = 487$  kJ/mol) > D9 (naphthacene;  $E_R = 460$  kJ/mol) > D8 (pyrene;  $E_R = 456$  kJ/mol) > D7 (phenanthrene;  $E_R = 381$  kJ/mol) > D6 (anthracene;  $E_R = 347$  kJ/mol) > D5 (naphthalene;  $E_R = 255$  kJ/mol).

### 3.1. Dyes Before Adsorption

#### 3.1.1. Degree of Planarity

As a result of the coplanarity of the dye's D- $\pi$ -A configuration, intramolecular charge transfer (ICT) can be ensured from one side to the other [17]. On the other side, an increase in the non-planarity of the donor unit of a dye is favorable, since self-aggregation can be significantly rendered [37]. Table 1 provides some of the major dihedral angles at different positions within the eight dyes. The dihedral angles (DA1) between the TPA units and the aromatic cores are in the range of 35.19 to 52.43°; the change in the DA2 represents the angle of rotation between the thiophene units; and the aromatic rings fall in a similar range, i.e., from 25.21 to 56.90°. These two ranges indicate a deviation from the planarity of these two regions within the molecules.

**Table 1.** The optimized dihedral angles (in °) (DA1, DA2, DA3, and DA4) of the eight investigated dyes.

Aromatic Core (Dye)	DA1 (TPA)	DA2 (TPH)	DA3 (ALKY1)	DA4 (ALKY2)
Anthanthrene (D2)	54.12	56.73	90.98	91.13
Naphthalene (D5)	35.40	25.61	92.34	90.97
Anthracene (D6)	35.22	25.66	91.82	93.71
Phenanthrene (D7)	36.21	56.21	179.21	88.77
Pyrene (D8)	52.63	46.95	86.64	91.85
Naphthacene (D9)	35.19	25.33	91.79	92.45
Chrysene (D10)	52.43	56.90	179.52	179.38
Perylene (D11)	36.44	28.10	179.15	179.30

On the other hand, the dihedral angles between the alkyl substituents and the aromatic cores show some variation, which can be attributed to the difference in the resonance energies of the aromatic cores since the alkyl chain in all molecules is the same (nonane). The degree of planarity is higher in three dye molecules, D7 (phenanthrene;  $E_R = 381$  kJ/mol); D10 (chrysene;  $E_R = 487$  kJ/mol); and D11 (perylene;  $E_R = 529$  kJ/mol). Since in these three dyes, DA3 and DA4 are very close to 180°, note that DA4 in D7 is 88.77°. All other dyes show an increase in out-of-plane distortion. It is worth mentioning that there is no direct relationship between the overall planarity of the molecule and resonance energies of the core aromatic rings.

To illustrate the degree of planarity of dye molecules, Figure 2 shows the dye molecules vertically. By looking at the orientations of the two alkyl groups in this figure, we can judge planarity. Figure 3 indicates that the D10 and D11 dye molecules showed more planarity compared to those of other dyes, since, in these two dyes, the two alkyl groups are coplanar with the aromatic cores. Also, to confirm this result, the molecular planarity parameter (MPP) was calculated [38]. MPP estimates the deviation of the whole molecular structure from the plane. Lower MPP values signify larger planarity. It is calculated utilizing the Multiwfn software (version 3.8) [39]. Accordingly, the planarity of the investigated dyes can be ordered as follows: D11 > D10 > D7 > D8 > D6 > D5 > D9 > D2.

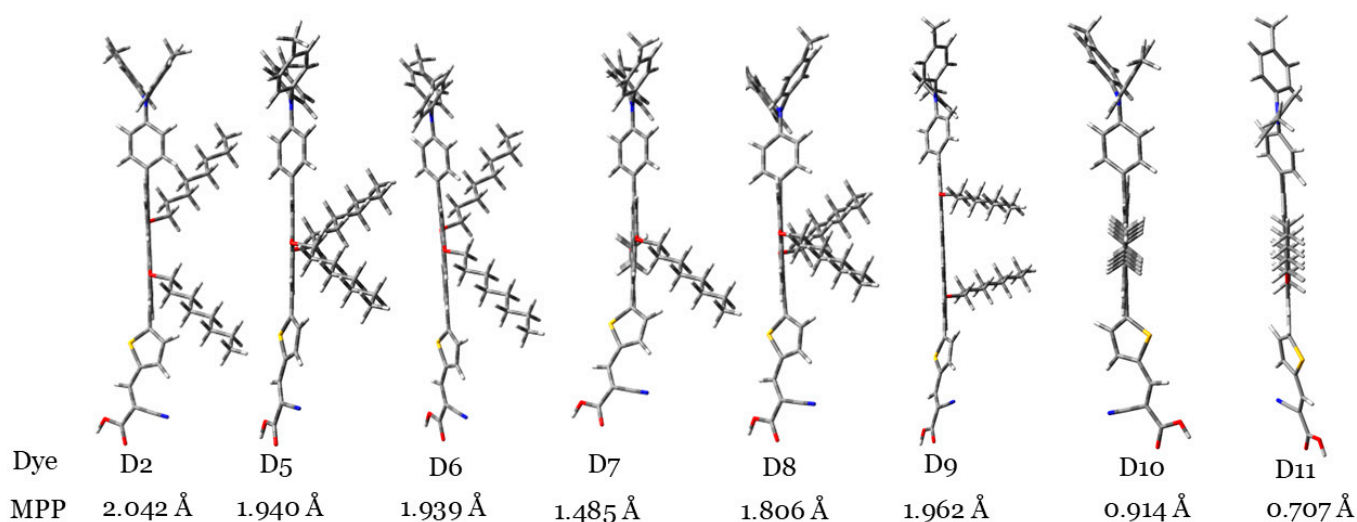


**Figure 3.** The investigated dyes are placed vertically to illustrate the degree of planarity of each dye molecule with respect to other dye molecules. MPP values also are indicated, and different atoms are indicated with different colors (S: yellow, N: blue, C: gray, O: red, H: white).

### 3.1.2. Frontier Molecular Orbitals (FMOs)

In Figure 4, at the CPCM/M06-2x/6-31+G(d,p) level of the theory, the FMO energy levels of the designed dyes (D5 to D11) are shown, along with those of the experimentally tested dye (D2) in the THF solvent. On the other hand, the alignment of the HOMO and LUMO energy levels of the TPA (triphenylamine), TPH (thiophene), and different  $\pi$ -bridge cores of the eight investigated dyes are discussed in the Supplementary Data (section: Additional Results and Discussion) and are illustrated in Figure S1. The designed dyes, with the appropriate HOMO and LUMO energies, aligned quite well with the redox potential (RP) of the  $I^-/I_3^-$  electrolyte ( $-4.8$  eV) [40] and the CB of  $TiO_2$ , in the present calculations,  $E_{CB}^{TiO_2} = -4.0$  eV [41,42]. Accordingly, the dyes designed are predicted to perform well during the key processes, i.e., dye regeneration and electron injection.

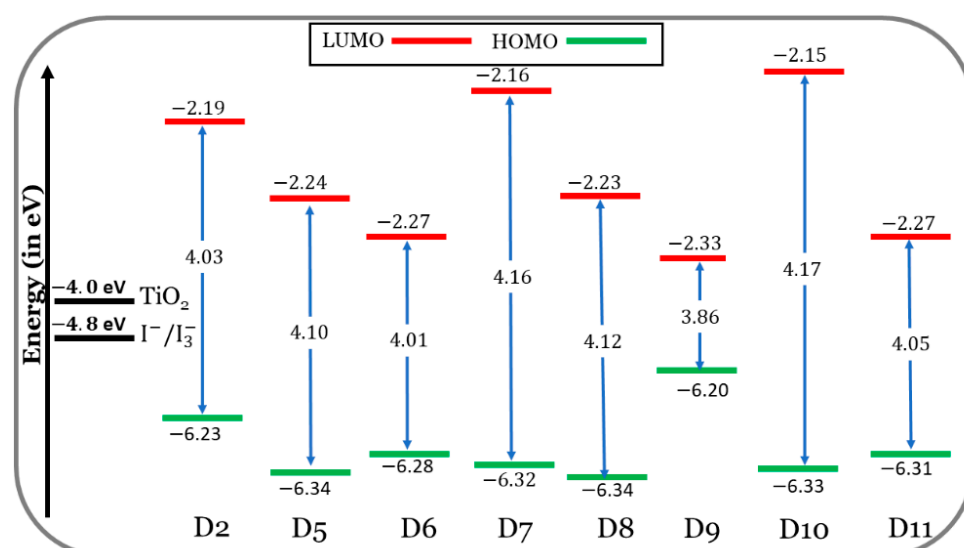


**Figure 4.** FMO energy levels of the seven designed dyes (D5 to D11) along with those of the efficient existing dye D2.

If the dye's LUMO energy is above the semiconductor's CB edge, this indicates that electrons are transferred from the excited state to the semiconductor in a favorable way. The LUMO levels of the designed dyes are situated in better positions compared to those

of the D2 dye. In other words, the LUMOs of the designed dyes are above and much closer to the CB of  $\text{TiO}_2$ . The electron injection from a closer LUMO is more thermodynamically favorable than from a farther LUMO level.

As compared to D2, the HOMOs of the designed dyes are lower in energy. An exception is the D9 dye. So, it is predicted that the dye regeneration process will be better for D2 compared to the designed dyes, and the D9 dye will be better than the D2 dye.

The energy gap is defined as follows:  $\Delta_{L-H} = E_{\text{LUMO}} - E_{\text{HOMO}}$ . It is expected that lower energy gaps will favor ICT within the dye molecule's skeleton and redshift, its absorption maxima. The values of  $\Delta_{L-H}$  decrease in the following order: D10 (4.17 eV) > D7 (4.16 eV) > D8 (4.12 eV) > D5 (4.10 eV) > D11 (4.05 eV) > D2 (4.03 eV) > D6 (4.01 eV) > D9 (3.86 eV). Only the D6 and D9 dyes (especially D9) show smaller energy gaps than the D2 dye, which means easier electron excitation and longer absorption wavelengths. This is evident in Section 3.1.3.

### 3.1.3. UV-Vis Spectroscopic Properties

In experiments, the D2 dye showed two absorption bands in the UV and Vis regions [15]. The UV band is more intense and is found at 329.77 nm, while the Vis-band intensity is lower at 460.36 nm. The difference between the calculated and experimental values of this dye is only 9 nm in the Vis band and only 21 nm in the UV band. Therefore, the calculated absorption wavelengths, as well as the level of theory used to calculate them (CPCM/TDCAM-B3LYP/6-31+G(d,p)), are reliable.

As with the D2 dye, the absorption spectra of dyes D5 to D11 also consist of two main bands. One ranges from 281.66 nm to 368.70 nm (UV region), and there is another band in the Vis region (in the range of 393.40 nm to 436.19 nm) (see Figure 5 and Table 2). Opposite to the oscillation strength values obtained for the four experimentally tested dyes in [15], here (the seven designed dyes), the  $f$  values of the Vis bands are larger than those of the UV region; therefore, the Vis bands are more intense than the UV bands. Because most solar light belongs to the visible and near-infrared ranges, this result is more beneficial [43]. As a general note, the  $\lambda_{\text{abs}}^{\text{calc}}$  values of the designed dyes become redder and shifted (longer wavelengths) as the resonance energies of the aromatic rings increase. This has also been proven in the literature [17,44]. This conclusion is shown in Figure 6.

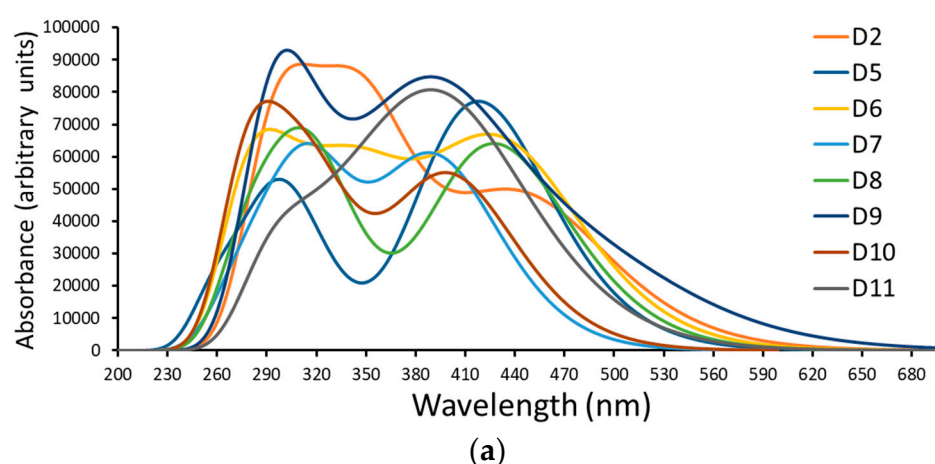
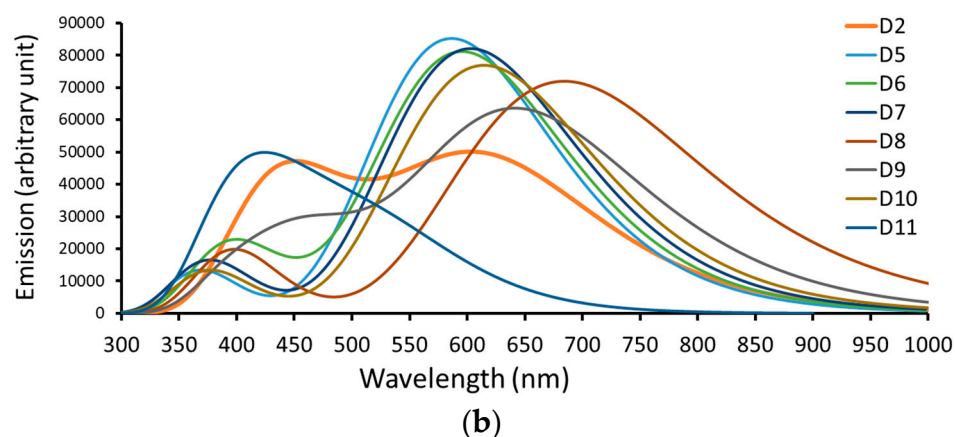


Figure 5. Cont.



**Figure 5.** A simulation of the (a) absorption spectrum and (b) emission spectrum of dyes D2 and D5 to D11.

**Table 2.** Computed absorption data and the distribution patterns of the FMOs of the isolated dyes D2 and D5 to D11 at the ground states involved in the major transition. Note: data on the D2 dye were collected from ref. [14].

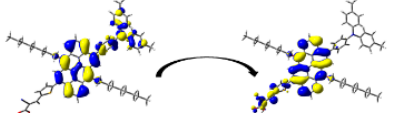
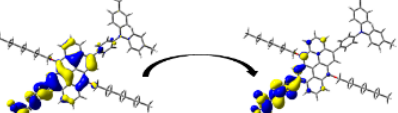
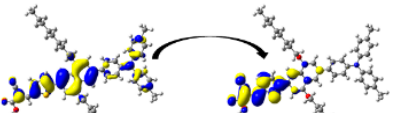
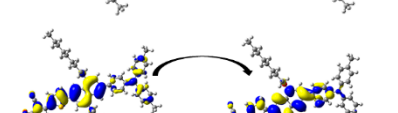
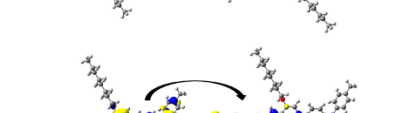
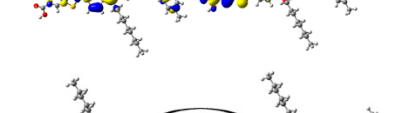
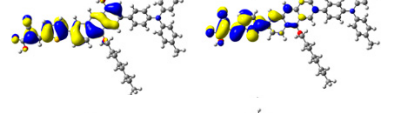
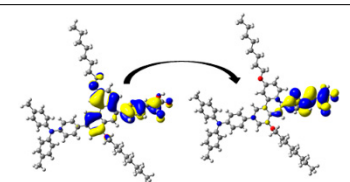
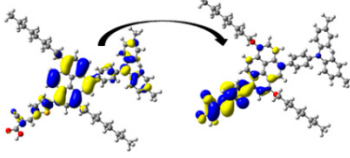
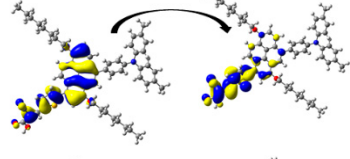
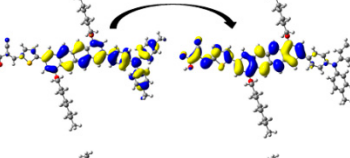
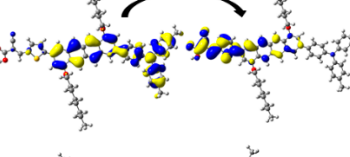
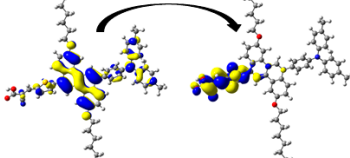
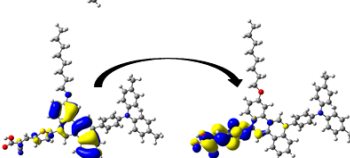
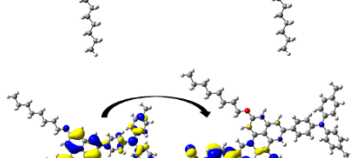
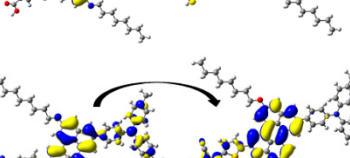
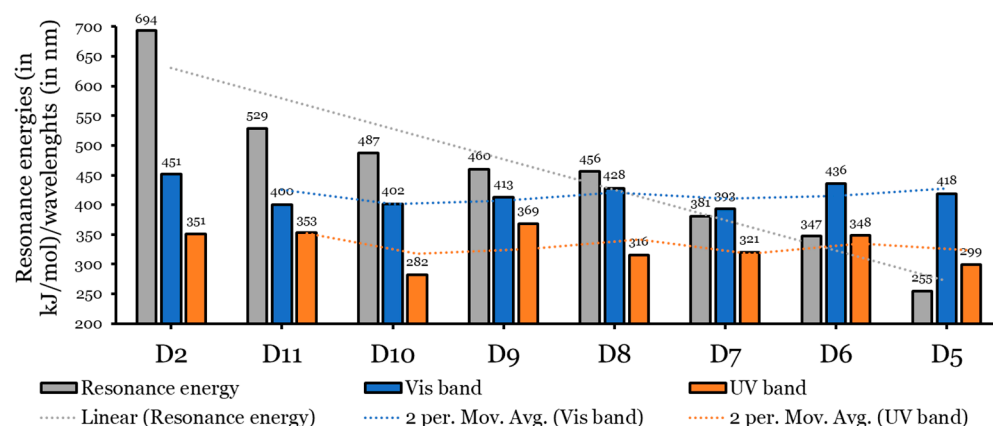
Dye	$\lambda_{\text{abs}}^{\text{calc}}$ (in nm/eV)	f	Transition	Transition Character	LHE	Iso-Density
D2	451.36/ 2.75	1.001	S0 $\rightarrow$ S1	H $\rightarrow$ L + 1 (49%)	0.900	
	350.77/ 3.53	1.490	S0 $\rightarrow$ S4	H-2 $\rightarrow$ L (47%)	0.968	
D5	418.47/ 2.96	1.899	S0 $\rightarrow$ S1	H-1 $\rightarrow$ L (50%)	0.987	
	299.41/ 4.14	0.4512	S0 $\rightarrow$ S6	H-1 $\rightarrow$ L + 1 (38%)	0.646	
D6	436.19/ 2.84	1.447	S0 $\rightarrow$ S1	H-1 $\rightarrow$ L (44%)	0.964	
	348.16/ 3.56	0.693	S0 $\rightarrow$ S3	H-2 $\rightarrow$ L (34%)	0.797	
D7	393.40/ 3.15	1.421	S0 $\rightarrow$ S1	H-1 $\rightarrow$ L (47%)	0.962	



Table 2. Cont.

Dye	$\lambda_{\text{abs}}^{\text{calc}}$ (in nm/eV)	f	Transition	Transition Character	LHE	Iso-Density
D8	320.55/ 3.87	0.863	S0 $\rightarrow$ S3	H-3 $\rightarrow$ L (32%)	0.863	
	428.01/ 2.90	1.571	S0 $\rightarrow$ S1	H-1 $\rightarrow$ L (50%)	0.973	
	315.51/ 3.93	0.830	S0 $\rightarrow$ S5	H-2 $\rightarrow$ L (27%)	0.852	
D9	413.38/ 3.00	1.289	S0 $\rightarrow$ S2	H $\rightarrow$ L + 1 (41%)	0.949	
	368.70/ 3.36	1.118	S0 $\rightarrow$ S3	H-1 $\rightarrow$ L (33%)	0.924	
D10	401.63/ 3.09	1.306	S0 $\rightarrow$ S1	H-1 $\rightarrow$ L (47%)	0.951	
	281.66/ 4.40	0.822	S0 $\rightarrow$ S10	H-2 $\rightarrow$ L (39%)	0.849	
D11	400.40/ 3.10	1.210	S0 $\rightarrow$ S2	H-1 $\rightarrow$ L (34%)	0.938	
	352.90/ 3.51	0.623	S0 $\rightarrow$ S4	H $\rightarrow$ L + 1 (44%)	0.762	

HOMO: H; LUMO: L.



**Figure 6.** Graphical presentation of the relationship between the  $\pi$ -aromatic's resonance energies and wavelengths in Vis and UV absorption bands.

The oscillation strengths of the Vis bands are in the range of 0.938 to 0.987, while the values of the UV bands are in the range of 0.762 to 0.924. Compared with D2, the Vis bands of the designed dyes are slightly blue-shifted. Despite this, as we mentioned previously, they have better oscillation strengths and thus higher LHEs which enhance the  $J_{sc}$  values [45]. In addition, the transition character is attributed to molecular orbitals other than the LUMO and HOMO orbitals, implying that ICT is the predominant factor affecting these transitions rather than  $\pi \rightarrow \pi^*$  transitions. The charge density of the FMOs of isolated dyes involved in the major transitions is illustrated in Table 2.

Table 3 lists the computed emission data calculated at CPCM/TDCAM-B3LYP/6-31+G(d,p) in the THF solvent, and Figure 4 represents the data graphically. Like the experimentally tested dye (D2), light from the dyes emits in the Vis region. The emission bands are significantly red-shifted from the absorption bands. The Stokes shift ( $\lambda_{ss}$ ) values range from 131 nm (D11) to 256 nm (D8). Compared to the other dyes investigated, the larger  $\lambda_{ss}$  of the D8 dye predicts a larger difference between its ground and excited state geometries.

**Table 3.** Computed emission data based on the  $S_1$  states. Note: data on D2 dye were collected from ref. [14].

Dye	$\lambda_{\max}^{\text{em}}$ (in nm/eV)	$f_{\max}^{\text{em}}$	$\lambda_{ss}$ (in nm)	$\tau$ (in ns)
D2	616.27/2.01	1.1659	165	4.817
D5	586.50/2.11	2.1031	134	2.428
D6	595.63/2.08	2.0038	159	2.623
D7	602.82/2.06	2.0263	209	2.644
D8	684.28/1.81	1.7785	256	3.902
D9	646.00/1.92	1.5433	233	3.996
D10	614.64/2.02	1.8978	213	2.936
D11	531.15/2.33	0.5762	131	7.268

Table 3 shows  $\tau$  (lifetime of the excited state calculated by Einstein's transition probabilities [46]) values of the investigated dyes. In fact, by lengthening the  $\tau$  value, more electrons can be injected into  $\text{TiO}_2$ 's CB. The lifetime values of the photoexcited electron of the designed dyes are generally smaller than that of the D2 dye. An exception is D11 (perylene core with 529 kJ/mol resonance energy). The lifetimes of the photoexcited electron followed the order D11 (7.268 ns) > D2 (4.817 ns) > D9 (3.996 ns) > D8 (3.902 ns) > D10 (2.936 ns) > D7 (2.644 ns) > D6 (2.623 ns) > D5 (2.428 ns); hence, the electron injection process becomes less feasible in the same order.

### 3.1.4. Reorganization Energies, Transfer Integrals, and Intrinsic Mobility

According to the Marcus electron transfer theory [47], for charge-transfer kinetics, a smaller reorganization energy gives rise to a higher rate constant. Figure 7 represents a bar plot of the electron and hole reorganization energies of the eight investigated dyes (D2 and D5 to D11) in THF, and detailed data are listed in Table S1.

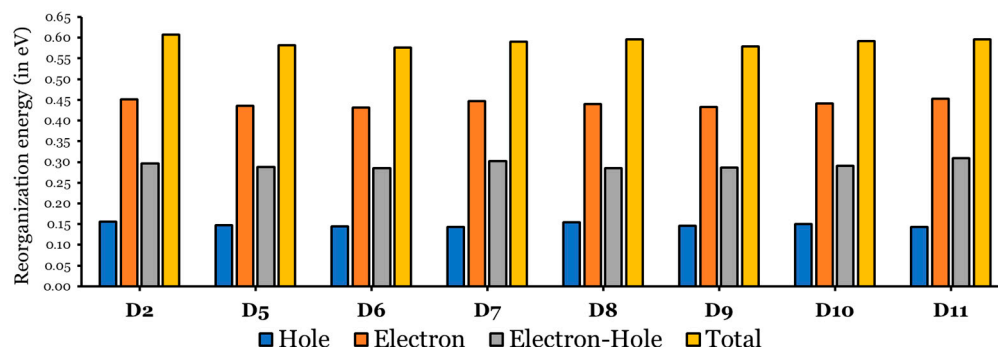


**Figure 7.** Reorganization energies of hole, electron, electron–hole, and total for D2 and D5 to D11 in THF.

The  $\lambda_{\text{elec}}$  values are much greater than the  $\lambda_{\text{hole}}$  values, indicating that the ability of all investigated dyes to transport holes is much better than their ability to transfer electrons [30,48], since  $\lambda_{\text{elec}}$  values ranged between 0.431 eV and 0.453 eV, while the range of  $\lambda_{\text{elec}}$  values are from 0.143 eV to 0.156 eV. Note that both regions are small.

In comparison to the D2 dye, the ability of the designed dyes to transfer holes is better than that of the D2 dye, since the  $\lambda_{\text{hole}}$  values (range from 0.143 to 0.155 eV) of the designed dyes are smaller than the  $\lambda_{\text{hole}}$  value of D2 (0.156 eV). In addition, the designed dyes (except D11 ( $\lambda_{\text{elec}} = 0.453$  eV)) can transfer electrons better than the D2 dye ( $\lambda_{\text{elec}} = 0.452$  eV), since the  $\lambda_{\text{elec}}$  values are within the range of 0.431 eV to 0.447 eV. Therefore, the designed dyes, having cores with smaller resonance energies, showed a better charge-transfer ability than the D2 dye [44]. Among the designed dyes, D6 shows the smallest  $\lambda_{\text{elec}}$ , and D11 shows the smallest  $\lambda_{\text{hole}}$ ; thus, they are predicted to perform the best as electron and hole transporter, respectively.

Additionally, the designed dyes showed better optimal electron–hole transport and smaller  $\Delta\lambda$  values. For D2,  $\Delta\lambda = 0.296$  eV, while the  $\Delta\lambda$  values for the designed dyes are in the range of 0.286 eV to 0.291 eV. The exceptions are D7 ( $\Delta\lambda = 0.303$  eV) and D11 ( $\Delta\lambda = 0.310$  eV). Also, the total reorganization energy ( $\lambda_{\text{tot}} = \lambda_{\text{hole}} + \lambda_{\text{elec}}$ ) values were calculated (see Figure 7 and Table S1). The  $\lambda_{\text{tot}}$  values of the dyes become smaller as the separation between the electron and hole becomes more effective. Due to this, recombination processes are rendered [45], and all the designed dyes have smaller  $\lambda_{\text{tot}}$  values compared to that of the D2 dye.

Based on the semi-classical model of the Marcus charge transfer [47,49], and by taking into account the  $\pi$ – $\pi$  stacking configuration between two neighboring dye molecules (dimer), see Figure 8, one can calculate key parameters, including the following: (1) the charge-transfer rate (denoted by  $k_{\text{CT}}^{+/-}$ ); (2) the electronic coupling matrix element ( $V_-$ ) and holes ( $V_+$ ) between two dye molecules; and (3) hopping mobility ( $\mu_{\text{hop}}^{+/-}$ ), which helps calculate the dye's electron or hole transport character. As can be seen in Table 4, these data are presented for each of the eight dye molecules investigated.

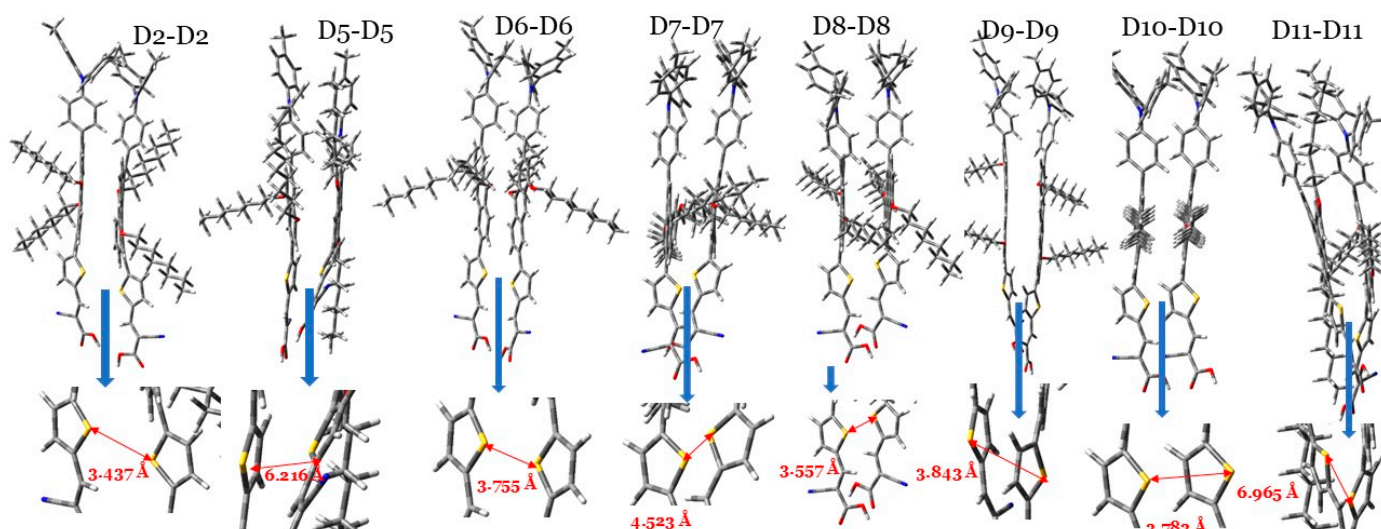


**Figure 8.** The optimized  $\pi$ -stacking arrangement of two adjacent dye molecules of the investigated dyes calculated at the CPCM/M06-2x/6-31+G(d,p) in THF. Note: the arrow between the two sulfur atoms (yellow) of the thiophene units is considered to represent the space distance between two interacting dye molecules.

**Table 4.** Charge-transfer rate parameters between two dyes in the  $\pi$ -stacking configuration include the electronic coupling matrix element  $V_{+}$  (in eV), the charge-transfer rate  $k_{CT}^{\pm}$  (in  $s^{-1}$ ), the space distance  $l$  (in Å), and hopping mobility  $\mu_{hop}^{\pm}$  (in  $cm^2 V^{-1} s^{-1}$ ).

Dye	$V_{+}$	$V_{-}$	$k_{CT}^{+} \times 10^{13}$	$k_{CT}^{-} \times 10^{13}$	$l$	$\mu_{hop}^{+}$	$\mu_{hop}^{-}$
D2	0.114	0.066	12.127	0.135	3.437	2.791	0.031
D5	0.053	0.064	2.886	0.152	6.216	2.172	0.114
D6	0.030	0.068	0.970	0.179	3.755	0.266	0.049
D7	0.056	0.068	3.419	0.152	4.523	1.362	0.061
D8	0.070	0.027	4.617	0.026	3.557	1.138	0.006
D9	0.023	0.119	0.539	0.535	3.843	0.155	0.154
D10	0.021	0.005	20.560	0.158	3.783	5.732	0.044
D11	0.015	0.028	0.238	0.026	6.965	0.225	0.023

The hole/electronic coupling matrix element ( $V_{+/-}$ ) of the dimer describes the coupling strength of hole–hole interactions/electron–electron interactions. These interactions strongly influence carrier mobility and charge transport rates [50,51]. A higher value of  $V_{+/-}$  is beneficial for charge transport when the coupling strength is high, because it increases charge mobility. For the dye molecules (D2, D8, D9, and D10) where  $V_{+} < V_{-}$ , this indicates that the coupling strength of electron–electron interactions is larger than the hole–hole interactions. In this way, the electron mobilities of these dyes are much higher than the hole mobilities. The reverse is true with respect to the other dyes, i.e., D5–D7 and D11.

The hole transfer rate ( $k_{CT}^{+}$ ) and electron transfer rate ( $k_{CT}^{-}$ ) values depend on two key parameters, and they are the hole/electronic coupling matrix element ( $V_{+/-}$ ) and hole and electron reorganization energies ( $\lambda_{+/-}$ ), as the molecule has a smaller  $\lambda_{+/-}$  and a larger  $V_{+/-}$ , as it will have a larger  $k_{CT}^{+/-}$  value [50,52]. For most of the investigated dyes, including D2,  $k_{CT}^{+} \gg / > k_{CT}^{-}$ , since the  $k_{CT}^{+}$  values range from  $0.970 \times 10^{13}$  to  $20.560 \times 10^{13} s^{-1}$ , while the  $k_{CT}^{-}$  values range from  $0.026 \times 10^{13}$  to  $0.179 \times 10^{13} s^{-1}$ . Hence, the hole transfer rate is much better than the electron transfer rate in these dyes. These dye molecules will act better as hole-transporting materials than electron-transporting materials. These results are in accordance with the calculated  $\lambda_{+/-}$  values of these dyes.

However, for D9,  $k_{CT}^+$  ( $0.539 \times 10^{13}$ ) is larger but very comparable to its  $k_{CT}^-$  ( $0.535 \times 10^{13}$ ). Considering this, the D9 dye has a distinct advantage in that its electron and hole charge rates are comparable. The space distance ( $l$ ) was measured as the distance between the two sulfur atoms in the two thiophene rings. Keep in mind that the  $\pi$ - $\pi$  stacking configuration of the core aromatic rings implies that their  $x$  and  $y$  coordinates are very similar. The  $l$  values of most dye dimers are comparable and close to 3 Å. Mainly due to steric hindrance, the increase in  $l$  values followed the following order: D2 (3.437 Å) < D8 (3.557 Å) < D6 (3.755 Å) < D10 (3.783 Å) < D9 (3.843 Å) < D7 (4.523 Å) < D5 (6.216 Å) < D11 (6.965 Å).

The hopping mobility of the hole ( $\mu_{hop}^+$ ) of the D2 dye dimer is greater than those of most other dye dimers, except the D7, D8, and D10 dye dimers. Meanwhile, the hopping mobility of the electrons ( $\mu_{hop}^-$ ) of the D2 dimer is smaller than most other dye dimers, except the D8 and D11 dye dimers. We should point out here that the hopping mobilities of each dye for electrons and holes are significantly different. For instance, for the D8 dye dimer,  $\mu_{hop}^+ = 1.138 \text{ cm}^2 \text{ V}^{-1} \text{ s}^{-1}$  is higher than its  $\mu_{hop}^-$  value by  $1.4 \text{ cm}^2 \text{ V}^{-1} \text{ s}^{-1}$ . However, this is not the case concerning the D9 dye dimer, since its hole and electron hopping mobilities are very similar and equal  $\sim 1.5 \text{ cm}^2 \text{ V}^{-1} \text{ s}^{-1}$ . The D9 dye dimers have equal electron and hole hopping mobilities, as we concluded previously concerning its charge-transfer rates. The dye in a DSSC has a dual role: the oxidized state of the dye transfers electrons to the CB of  $\text{TiO}_2$ , and the unoxidized state of the dye transfers holes to the electrolyte. The balanced ability to transfer the hole and electron of a dye gives an advantage for the total performance of this dye, which is the case for the D9 dye dimer.

Johnson et al. [53] suggested the noncovalent interaction (NCI) approach. We can determine the types and regions of weak interactions in molecular systems by analyzing the electron density and its derivatives. This method represents van der Waals (VDW), steric clashes, and hydrogen bonds using only atomic coordinates as the input [53]. A gradient isosurface is colored according to the values of  $\text{sign}(\lambda_2)\rho$ , and this is a good indicator of the strength of interactions. Large and negative values of  $\text{sign}(\lambda_2)\rho$  are revealing of an attractive interaction (such as hydrogen bonding/dipole-dipole), while a large and positive  $\text{sign}(\lambda_2)\rho$  is revealing of a nonbonding interaction. Values near zero reveal very weak VDW interactions.

The dye dimers were examined for their interaction. Two-dimensional scatter maps and 3D color-filled NCI-RDG isosurfaces of the D2–D2 and D5–D5 dimers at the CPCM/B3LYP-D/6-31G(d,p) in THF, as representative examples, are shown in Figure 9, and similar plots for the other dimers are found in Figure S3. A VDW interaction is indicated by the green region, a strong steric effect is indicated by the red region, and an H-bond attraction is indicated by the blue region. The 3D colored-filled RDG isosurfaces are more informative than the NCI-RDG 2D scatter maps (see Figures 8 and S3). Although the two monomer molecules are in a  $\pi$ - $\pi$  stacking arrangement, the aromatic cores face each other. The main interaction between them inside the dimer is due to VDW interactions (green plates), indicating the stability of such a configuration. As a result of the strong steric effect of aromatic rings, small red plates can be observed inside each of the monomer's aromatic rings.



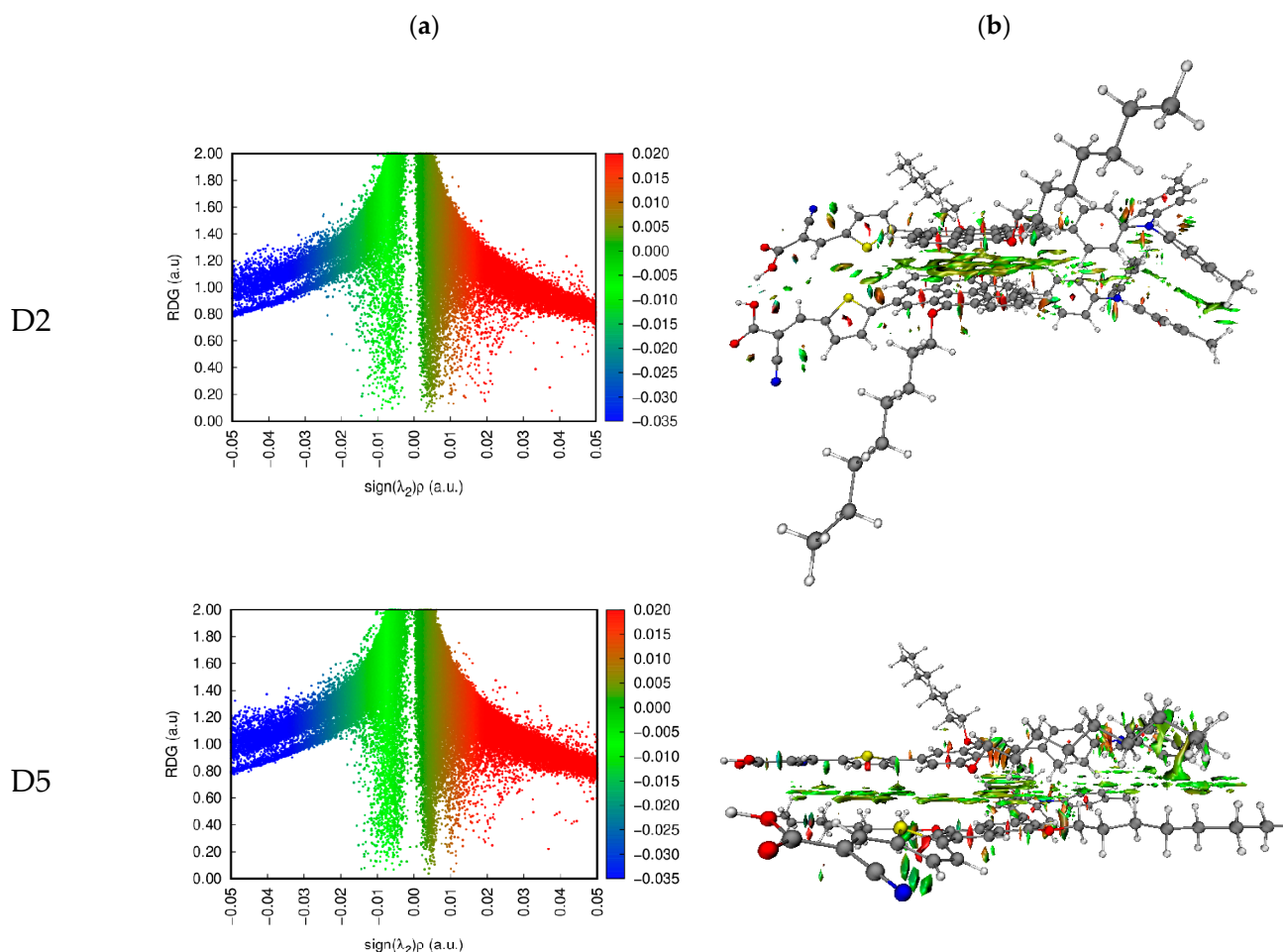


**Figure 9.** NCI isosurfaces: (a) 2D scatter maps and (b) 3D color-filled RDG isosurfaces of D2 and D5 dye dimers as representative examples at CPCM/M06-2x/6-31+G(d,p) in THF.

### 3.1.5. Le Bahers' Intramolecular Charge-Transfer Indices

Since we are dealing with dyes that differ in their  $\pi$ -bridge aromatic rings, it is beneficial to estimate the ICT indices utilizing the code created by Le Bahers et al. [54]. A light-to-electricity conversion of a DSSC is made more efficient by ICT. Since the dye adsorbed on a semiconductor surface absorbs light and separates electrons from holes, a DSSC creates an electron–hole separation. So, the distance between the hole (positive region) and electron (negative region) should be large to enhance the ICT. Le Bahers' model requires only the total electronic densities of the  $S_0$  and  $S_1$  states. The dye molecule can be considered as a push (D)–pull (A) rod-like molecule, and upon photoexcitation, the ground state ( $S_0$ ) D–A changes into an excited state ( $S_1$ )  $D^+A^-$ . Through DFT calculations, we can obtain the  $S_0$  density, and through TD-DFT calculations, we obtain the  $S_1$  density. The CT indices calculated at the CPCM/TDCAM-B3LYP/6-31+G(d,p) in THF are listed in Table S2 and are represented graphically in Figure 10.

In general, larger intramolecular distances increase the efficacy of a DSSC. The charge-transfer distance (D) values increase as follows: D5 (0.764 Å) < D2 (1.071 Å) < D9 (1.107 Å) < D8 (1.305 Å) < D6 (1.956 Å) < D11 (2.930 Å) < D7 (3.308 Å). There is no clear correlation between the resonance energies of  $\pi$ -aromatic cores and the spatial distance between the  $\rho^+$  and  $\rho^-$  regions associated with electronic excitation. In fact, the two cores with the maximum and minimum resonance energies, i.e., D2 and D5, respectively, recorded the lowest values of D. On the other hand, D7, with a phenanthrene core, recorded the largest value of D.

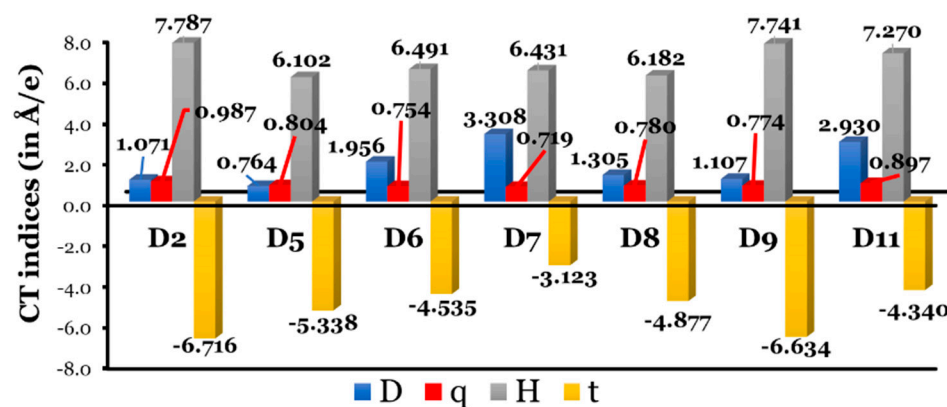


**Figure 10.** Graphical representation of Le Bahers' CT indices. Note: data for D10 dye were not converged and are not included.

The amount of charge-transferred ( $q$ ) values fall into small ranges, from 0.719 to 0.987 e, and increase as follows: D7 (0.719 e) < D6 (0.754 e) < D9 (0.774 e) < D8 (0.780 e) < D5 (0.804 e) < D11 (0.897 e) < D2 (0.987 e). Clearly, the dye with the largest charge separation ( $D$  value) has the smallest amount of charge transfer ( $q$  value). The opposite is true regarding the D2 dye, i.e., D2 recorded one of the smallest  $D$  values and the largest  $q$  value. However, we cannot generalize the inverse relationship between the  $D$  and  $q$  values for the other dyes.

For all investigated dyes, an overlap between the centroids along the axis of charge transfer is expected, since the  $H$  index is  $\gg D$ . Finally, the  $t$  index (quantify through-space excitations in ICTs) should satisfy three important criteria: (i) it should be smaller than 1.6 to accurately account for the transition energy [54–56]; (ii) it should be positive, since positive values of  $t$  are associated with a better separation between the areas of density increment and depletion, and (iii) an increase in the  $t$  value occurs with a reduced overlap between electron-donating and electron-accepting regions [57]. The recorded  $t$  values are all less than 1.6 and are negative, evidencing regions of high and low electron density overlap spatially [54,57]. The extent of overlap increases as the  $t$  values become more negative, and this follows the following order: D7 ( $-3.123$  Å) > D11 ( $-4.340$  Å) > D6 ( $-4.535$  Å) > D8 ( $-4.877$  Å) > D5 ( $-5.338$  Å) > D9 ( $-6.634$  Å) > D2 ( $-6.716$  Å). In D2 (with the largest  $E_R$ ), a region of high and low electron density overlaps the most, while all the designed dyes have a smaller overlap.

In conclusion, compared to the designed dyes and D2, the experimentally tested dye showed the smallest  $D$  value and the largest  $q$  and  $t$  values, which were unbeneficial for an effective ICT process. Thus, it is expected that the designed dyes will show better ICT characteristics. However, no clear relationship was detected between the  $E_R$  and CT index values.

A visual illustration of ICT by mapping the electron density variation between  $S_1$  and  $S_0$  is shown in Figure 10. In cyan, the electron density is decreased, while in blue, it is increased. From Figure 11, the electron density of the  $\pi$ -linker, thiophane, and cyanoacrylic acid units is highest for all dyes, whereas the electron density of the TPA unit is the lowest. In other words, the electron density is the highest in units with a  $\pi$ -linker and acceptor and the lowest in units with donors. Therefore, it can be concluded that during the electronic transition  $S_0 \rightarrow S_1$ , charges are transferred through the  $\pi$ -bridge from the donor to the acceptor [45].

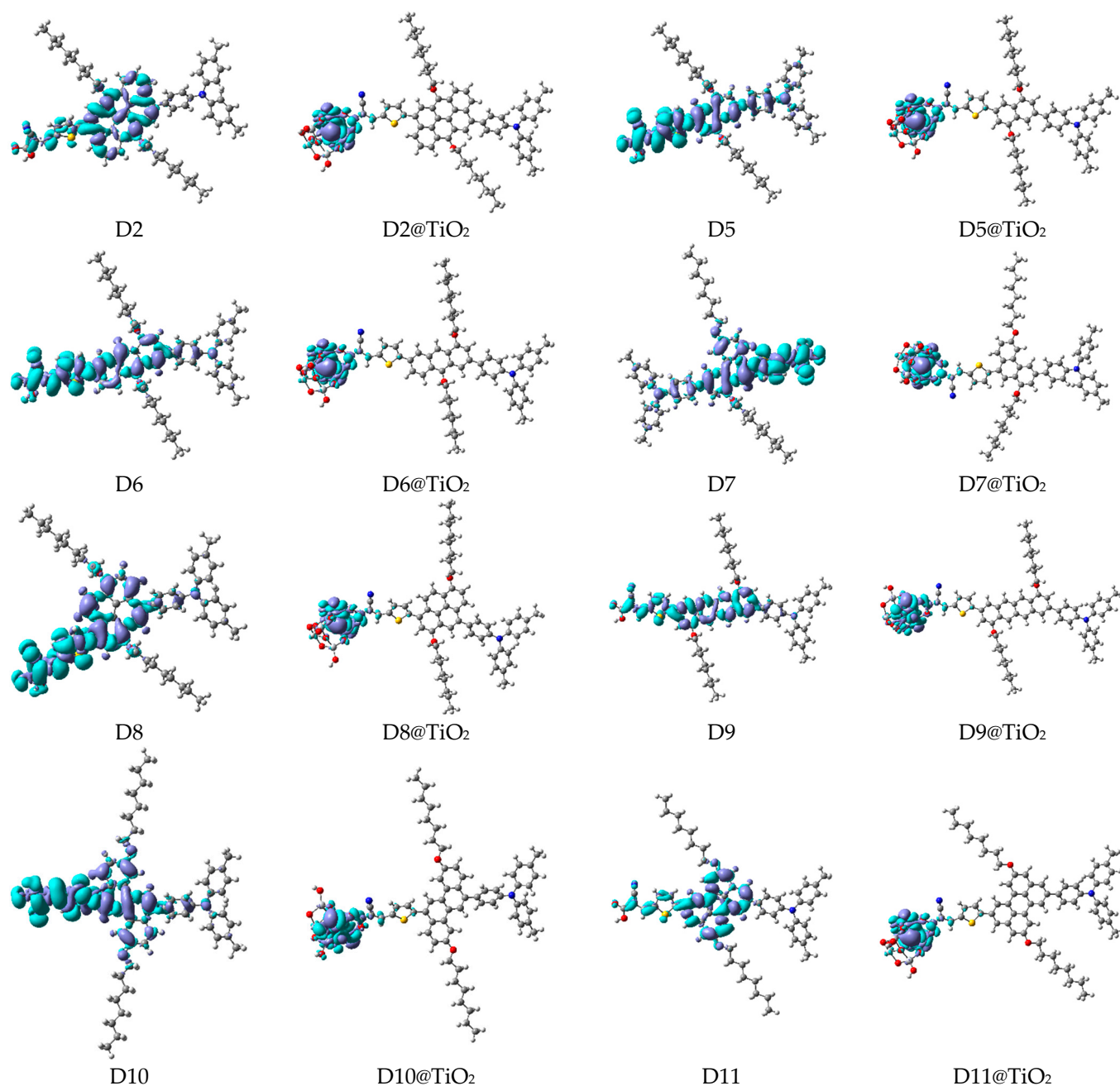


**Figure 11.** EDD plots between S<sub>1</sub> and S<sub>0</sub> states of the investigated dyes (isolated and adsorbed forms).

### 3.1.6. Electron Injection and Dye Regeneration Free Energies

Charge injection into the CB, followed by dye regeneration, is highly dependent on the difference between a dye's excited state oxidation potential (ESOP =  $E^{\text{Dye}^*}$ ) and TiO<sub>2</sub>'s CB, and the optimal value of the free energy of electron injection ( $\Delta G_{\text{inj}}$ ) is  $\geq 0.2$  eV [37,58,59]. Meanwhile, the optimal difference between a dye's ground-state oxidation potential (GSOP =  $E^{\text{Dye}}$ ) and an electrolyte's redox couple, the free energy of a dye regeneration, is  $\Delta G_{\text{reg}} \geq 0.4$  eV [37,58,59]. The values of the  $E^{\text{Dye}}$ ,  $E^{\text{Dye}^*}$ ,  $E_{\text{ex}}$ ,  $\Delta G_{\text{inj}}$ , and  $\Delta G_{\text{reg}}$  of the eight investigated dyes calculated in THF at CPCM/TDCAM-B3LYP/6-31G(d,p) are listed in Table S3, and the values of  $\Delta G_{\text{inj}}$  and  $\Delta G_{\text{reg}}$  are represented graphically in Figure 12. The  $\Delta G_{\text{inj}}$  values of the investigated dyes range from  $-0.504$  to  $-0.791$  eV ( $\gg 0.2$  eV, as required), and the  $\Delta G_{\text{reg}}$  values range from  $-1.436$  to  $-1.582$  eV ( $\gg 0.4$  eV, as required). Negative values of  $\Delta G_{\text{inj}}$  indicate that a dye has sufficient driving force to ensure electron injection into TiO<sub>2</sub>. According to Figure 11 and Table S3, all the designed dyes

have greater  $\Delta G_{\text{inj}}$  values than that of the D2 dye molecule, implying that the designed dyes have a considerably increased electron injection driving force [30,48,60,61]. The  $\Delta G_{\text{inj}}$  values increase (become more negative) as follows: D2 (−0.504 eV) < D6 (−0.516 eV) < D8 (−0.518 eV) < D5 (−0.582 eV) < D10 (−0.724 eV) < D11 (−0.750 eV) < D9 (−0.764 eV) < D7 (−0.791 eV).

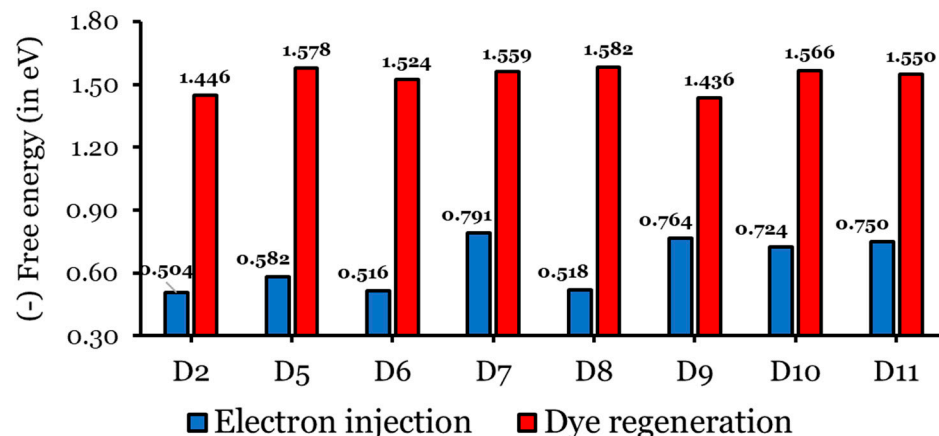


**Figure 12.** Electron injection and dye regeneration free energies (in eV) of the isolated dyes.

It is necessary to have enough of  $\Delta G_{\text{reg}}$  to achieve efficient regeneration. The  $\Delta G_{\text{reg}}$  values of the eight investigated dyes are all negative, indicating that the dye has sufficient driving force to ensure a smooth dye regeneration process by the electrolyte. Also, the designed dyes have greater  $\Delta G_{\text{reg}}$  values than that of the D2 dye molecule, implying that the designed dyes can considerably improve the process of dye regeneration. An exception is the D9 dye, which has a smaller  $\Delta G_{\text{reg}}$  value compared to that of the D2 dye. Consequently, we conclude that the dyes designed in this study are promising candidates for improving the photovoltaic properties of DSSCs.

### 3.2. Dyes After Adsorption on $\text{TiO}_2$ Clusters

It has been reported in the literature that either periodic models or clusters of  $\text{TiO}_2$  can be used to model dye@ $\text{TiO}_2$ -adsorbed systems. To achieve a successful simulation of the optoelectronic properties of the adsorbed system with a low computational cost, small clusters have been used [17,30,37,62]. This work considers the anatase  $(\text{TiO}_2)_6\text{H}_3$  cluster to simulate dye@ $\text{TiO}_2$  complexes [63–65]. In this study, the dyes bind almost perpendicular to the  $\text{TiO}_2$  surface. After deprotonating the hydrogen of  $-\text{COOH}$ , oxygen atoms are attached to  $\text{TiO}_2$  clusters through a bidentate bridging mode [30,66,67]; therefore, the two monomers in the adsorbed system will be connected by two Ti–O covalent bonds. These two covalent bonds are designated as (Ti–O)1 and (Ti–O)1. The adsorption energies ( $E_{\text{ads}}$ ) were calculated as follows:

$$E_{\text{ads}} = E_{\text{dye@TiO}_2} - [E_{\text{dye}} + E_{\text{TiO}_2}] \quad (2)$$

$E_{\text{dye@TiO}_2}$  is the energy of the optimized complex (dye@ $\text{TiO}_2$ ).  $E_{\text{dye}}$  and  $E_{\text{TiO}_2}$  are the energies of the optimized dye and  $\text{TiO}_2$  cluster, respectively. Reliable adsorption energy was obtained by adding hydrogen energies to the system.

It is safe to assume that stable adsorption occurs when the adsorption energy is negative, see Table S4, and the data in Table S4 is illustrated graphically in Figure 13. Table S5 lists the bond lengths of the two Ti–O bonds between the dye and  $\text{TiO}_2$  cluster. Table S5 shows that the bond lengths of these two bonds in the eight investigated dyes are very comparable and are approximately equal to  $\sim 2 \text{ \AA}$ . They are in the range of 2.0377 to

2.0652 Å. The obtained bond lengths are in the same range reported in other theoretical works for other dye@TiO<sub>2</sub>-adsorbed systems [37,45,68]. Hence, a chemisorption type of adsorption may occur in these adsorbed systems [45], and this conclusion is supported by the reported values of adsorption energies, as we will see in the next paragraph.

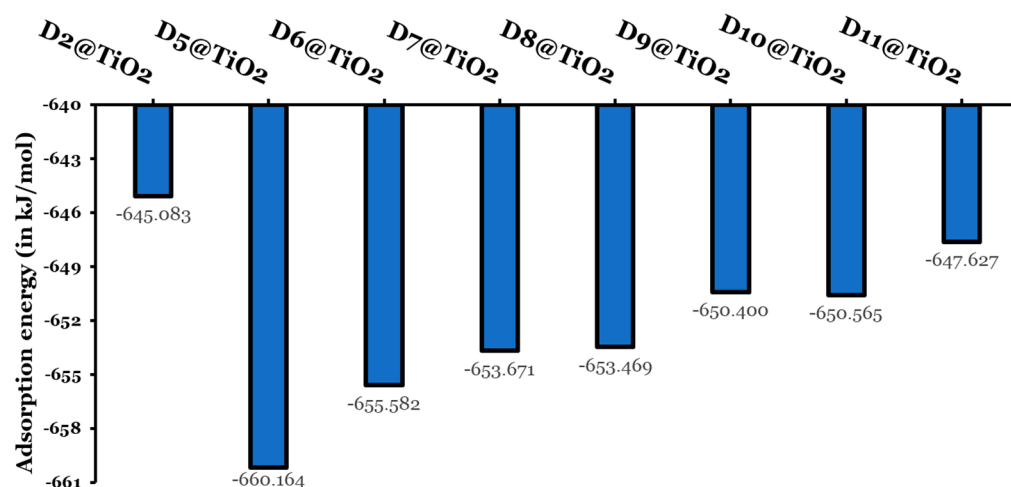


Figure 13. Adsorption energies (in kJ/mol).

The adsorption energies of the eight investigated dyes fall in the range of −645.083 to −660.164 kJ/mol. Larger adsorption energies indicate a chemisorption mechanism. In addition, larger adsorption energies are a sign of an increase in the electron transfer rate, leading to enhanced photovoltaic performance. The designed dyes reordered higher adsorption energies than the experimentally tested dye (D2). The D5@TiO<sub>2</sub>-adsorbed system reported the highest negative adsorption energy ( $E_{\text{ads}} = -660.164$  kJ/mol) and thus the most stable adsorbed system. The other adsorbed systems have larger (less negative) adsorption energies by not less than 4.6 kJ/mol and not more than 15.1 kJ/mol. The adsorbed systems can be arranged according to their increase in stability and decrease in their adsorption energies as follows: D2@TiO<sub>2</sub> (−645.083 kJ/mol) < D11@TiO<sub>2</sub> (−647.627 kJ/mol) < D9@TiO<sub>2</sub> (−650.400 kJ/mol) < D10@TiO<sub>2</sub> (−650.565 kJ/mol) < D8@TiO<sub>2</sub> (−653.469 kJ/mol) < D7@TiO<sub>2</sub> (−653.671 kJ/mol) < D6@TiO<sub>2</sub> (−655.582 kJ/mol) < D5@TiO<sub>2</sub> (−660.164 kJ/mol).

### 3.2.1. Optical Properties

The TiO<sub>2</sub> nanoparticle surface was modeled using a small cluster of Ti<sub>6</sub>O<sub>12</sub>H<sub>3</sub>. The band gap ( $\Delta_{\text{CB-VB}}$ ) of this cluster is 4.561 eV larger than 3.2 eV [69], and the experimental band gap of the TiO<sub>2</sub> anatase is due to the difference in size. However, the  $S_0 \rightarrow S_1$  optical gap was calculated to be 3.42 eV. The deviation (0.22 eV) is minor from the experimental value [69]. On the other hand, the obtained band gap is very close to the reported values of band gaps for other similar small clusters [30,37,45,62]. The HOMO–LUMO energy gaps ( $\Delta_{\text{L-H}}$ ) of isolated dyes are larger than the energy gaps of their adsorbed systems. The difference between the two datasets is not less than 0.081 eV nor more than 0.161 eV. This trend indicates an enhancement in the charge transport properties upon adsorption [45]. The  $\Delta_{\text{L-H}}$  values of adsorbed systems show a decrease in the following order: D10@TiO<sub>2</sub> > D7@TiO<sub>2</sub> > D8@TiO<sub>2</sub> > D11@TiO<sub>2</sub> > D5@TiO<sub>2</sub> > D6@TiO<sub>2</sub> > D2@TiO<sub>2</sub> > D9@TiO<sub>2</sub>. Hence, this is the order in which the charge-transfer ability increases. The shift of the CB of the semiconductor ( $\Delta_{\text{CB}}$ ) when the dye is adsorbed can be expressed using the following equation [70]:

$$\Delta_{\text{CB}} = \frac{q \cdot \mu_{\text{normal}} \cdot \gamma}{\epsilon_0 \epsilon} \quad (3)$$



where  $q$  is the electron charge,  $\gamma$  is the surface concentration of the dye molecule, the  $\mu_{\text{normal}}$  of a dye molecule isolated from a semiconductor surface has a dipole moment perpendicular to its surface, and  $\epsilon_0$  and  $\epsilon$  represent the vacuum permittivity and dielectric permittivity, respectively. On the other hand, the open-circuit voltage ( $V_{\text{oc}}$ ) can be calculated according to the equation below [70]:

$$V_{\text{oc}} = \left( \frac{E_{\text{CB}} + \Delta\text{CB}}{q} \right) + \left( \frac{k_{\text{B}}T}{q} \right) \ln \left( \frac{n_{\text{CB}}}{N_{\text{CB}}} \right) - \frac{RP}{q} \quad (4)$$

$q$  is the unit charge,  $E_{\text{CB}}$  is the conduction band edge of the semiconductor,  $k_{\text{B}}$  is the Boltzmann constant,  $T$  is the absolute temperature,  $n_{\text{CB}}$  is the number of electrons in CB, and  $N_{\text{CB}}$  is the density of accessible states in CB. Therefore, different dipole moments are anticipated to significantly affect the  $\Delta\text{CB}$  of  $\text{TiO}_2$ , which in turn will affect the value of  $V_{\text{oc}}$ . It has been reported that the higher the dipole moment ( $\mu_{\text{normal}}$ ) of the adsorbed dye pointing outward from the  $\text{TiO}_2$  surface, the larger the  $V_{\text{oc}}$  [71]. The  $\mu_{\text{normal}}$  values of the investigated dyes were calculated at the geometry of the dye adsorbed on  $\text{TiO}_2$ , and they are recorded in Table S6. Some of the designed dyes have larger  $\mu_{\text{normal}}$  values compared to that of the D2 dye. The  $\mu_{\text{normal}}$  value of the D2 molecule is 9.963 Debye, and for D5, D6, and D9, they are larger, by 0.158, 0.286, and 0.511 Debye, respectively. For the other designed dyes (D7, D8, D10, and D11), their  $\mu_{\text{normal}}$  values are smaller than the D2 dye, by 0.572, 0.608, 0.435, and 0.267 Debye, respectively. Therefore, it is expected the three designed dyes (D5, D6, and D9) with larger  $\mu_{\text{normal}}$  values will produce larger  $V_{\text{oc}}$  values compared to that of the D2 dye in a DSSC device. Of course, this is a general prediction, since other factors are affecting the  $V_{\text{oc}}$  values, such as the charge distribution at the  $\text{TiO}_2$  surface [70].

Alternatively, the ground-state dipole moments of the  $\text{TiO}_2$ - and dye@ $\text{TiO}_2$ -adsorbed systems are also presented in Table S6. As we can see, the dipole moment of  $\text{TiO}_2$  is only 1.941 Debye, and after the adsorption process, the dipole moments of the dye@ $\text{TiO}_2$ -adsorbed systems are elevated to a great extent, ranging from 5.847 to 10.674 Debye. In addition, the dipole moments of the three adsorbed systems, D5@, D6@, and D8@ $\text{TiO}_2$ , are larger than their isolated dyes, indicating an elevation in their charge transport properties [45].

Figure S4 represents the total density-of-states (TDOS) plots of the dye@ $\text{TiO}_2$ -adsorbed systems. We did not consider the partial DOS (PDOS) from each component in the dye@ $\text{TiO}_2$  systems, i.e., dye and  $\text{TiO}_2$ , because the PDOS of a dye is expected to have a minor contribution to the TDOS [72,73]. The energy gaps ( $\Delta_{\text{L-H}}$ ) of dye@ $\text{TiO}_2$  fall in a small region and decrease in the following order: D10@  $\text{TiO}_2$  (4.053 eV) > D7@  $\text{TiO}_2$  (4.000 eV)  $\geq$  D8@  $\text{TiO}_2$  (3.990 eV) > D5@  $\text{TiO}_2$  (3.984 eV) > D11@  $\text{TiO}_2$  (3.945 eV) > D6@  $\text{TiO}_2$  (3.905 eV) > D2@ $\text{TiO}_2$  (3.883 eV) > D9@ $\text{TiO}_2$  (3.782 eV). This order indicates the order of increasing ICT properties of the dye@ $\text{TiO}_2$  systems with respect to each other.

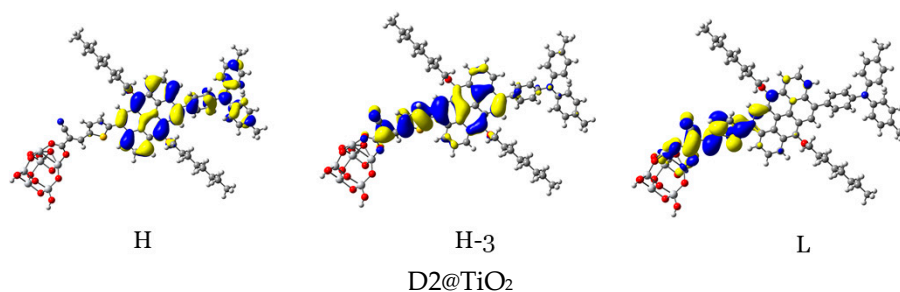
The electronic absorption spectra of the dyes on the  $\text{TiO}_2$  substrate were examined using CPCM/TDCAM-B3LYP with 6-31+G(d,p) and LANL2DZ in THF. This study aims to investigate the relationship between spectroscopic properties and solar energy conversion efficiency. The UV-Vis absorption properties of the dye@ $\text{TiO}_2$  systems, such as the maximum wavelengths/energies and their oscillation strengths, transition, transition characters, and LHEs, are recorded in Table 5. A simulation of the absorption spectra is shown in Figure S5. Upon adsorption, the two maximum wavelengths are shifted to longer wavelengths (red-shift) for some dye@ $\text{TiO}_2$  systems and to shorter wavelengths (blue-shift) for other dye@ $\text{TiO}_2$  systems compared to the values of their isolated dyes. However, in all cases, the change (elongation or shortening) in the wavelengths is small and does not exceed 13 nm/0.11 eV. Similar to the observed red-shift in wavelengths with increasing  $\pi$ -linker resonance energies for isolated dyes, this trend is also evident in the values associated with adsorbed systems. The aromatic core of the D2 dye has the maximum resonance

energy, showing maximum absorption wavelengths in the UV and Vis regions. The two maximum wavelengths of all other designed systems are shorter. The changes in the absorption spectra of the adsorbed dyes, including changes in intensity and shape, may result from the aggregation of dye molecules at the TiO<sub>2</sub> surface. This aggregation may occur either through an H-type or a J-type aggregation, depending on the orientation of the dye molecules.

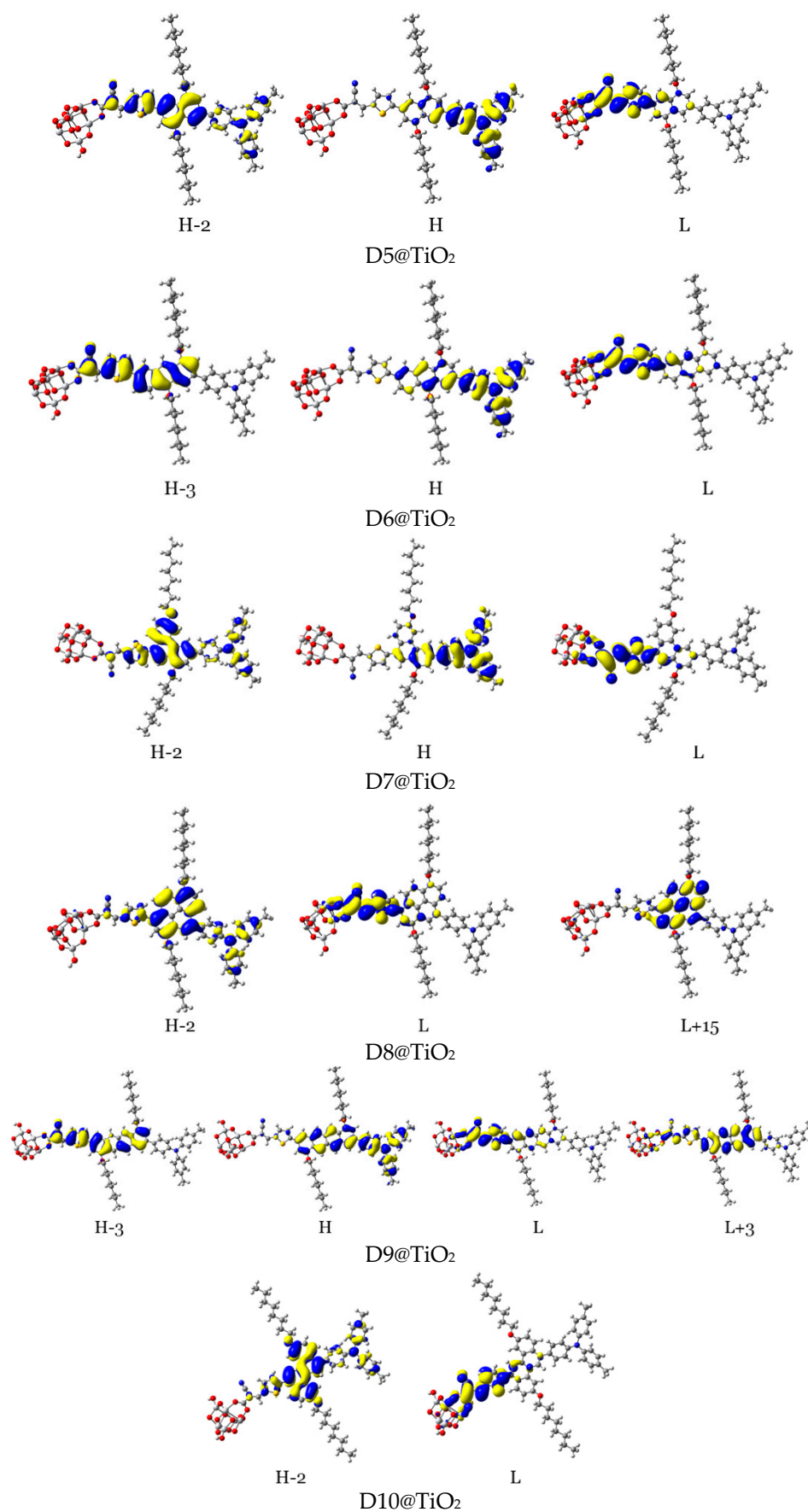
**Table 5.** Computed absorption data of dye@TiO<sub>2</sub> systems. Note: data on D2 dye were collected from ref. [14].

Dye@TiO <sub>2</sub>	$\lambda_{\text{abs}}^{\text{calc}}$ (in nm/eV)	f	Transition	Transition Character	LHE
D2@TiO <sub>2</sub>	442.53/2.802	0.863	S0 → S9	H → L (51%)	0.863
	357.25/3.471	0.726	S0 → S16	H-3 → L (45%)	0.812
D5@TiO <sub>2</sub>	415.65/2.983	1.9869	S0 → S10	H-2 → L (48%)	0.990
	307.09/4.037	0.3834	S0 → S20	H → L (38%)	0.586
D6@TiO <sub>2</sub>	434.58/2.853	1.6115	S0 → S9	H → L (43%)	0.976
	347.24/3.571	0.5086	S0 → S9	H-3 → L (41%)	0.690
D7@TiO <sub>2</sub>	415.73/2.982	1.5539	S0 → S10	H-2 → L (46%)	0.972
	313.00/3.961	0.9301	S0 → S9	H → L (30%)	0.883
D8@TiO <sub>2</sub>	431.15/2.876	1.5860	S0 → S10	H-2 → L (47%)	0.974
	315.21/3.933	0.4721	S0 → S19	H-2 → L+15 (28%)	0.663
D9@TiO <sub>2</sub>	409.02/3.031	1.0321	S0 → S11	H → L+3 (40%)	0.907
	366.16/3.386	1.0507	S0 → S15	H-3 → L (33%)	0.911
D10@TiO <sub>2</sub>	410.60/3.020	1.2562	S0 → S10	H-2 → L (45%)	0.945
	319.47/3.881	0.7682	S0 → S18	H-2 → L (35%)	0.829
D11@TiO <sub>2</sub>	397.18/3.122	1.4398	S0 → S13	H-1 → L+4 (35%)	0.964
	365.14/3.396	0.4673	S0 → S19	H-3 → L (46%)	0.659

For efficient sensitization, it is required that the electron density of the highest occupied molecular orbitals (HOMO, HOMO-1, and other adjacent HOMOs) be located on or nearby the dye's donor units, while that of the lowest unoccupied molecular orbitals (LUMO, LUMO+1, and other adjacent LUMOs) be distributed on the acceptor units and be close to the semiconductor moiety. In Table 5 and Figure 14, the density of charge of the dye@TiO<sub>2</sub> clusters participating in the most important transitions is depicted. The major electronic transitions are attributed to HOMO/HOMO-1/HOMO-2/H-3 and to LUMO/LUMO + 2/LUMO + 3 molecular orbitals.



**Figure 14.** Cont.

Figure 14. *Cont.*

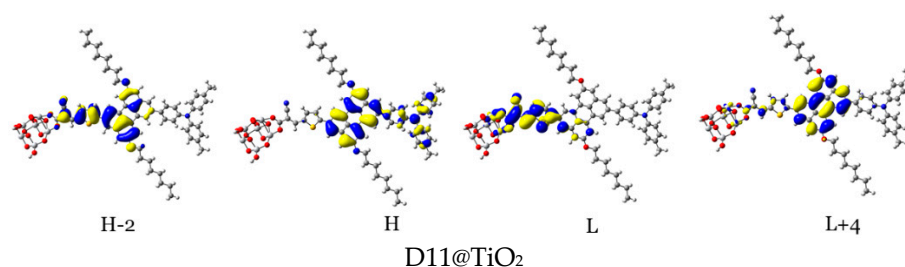


**Figure 14.** Distribution patterns of the FMOs of the D2 and D5 to D11 adsorbed on  $\text{TiO}_2$  clusters involved in the most important transition (see Table 5).

In the  $\text{D2@TiO}_2$  system, the most important transitions are from  $\text{H} \rightarrow \text{L}$  and  $\text{H}-3 \rightarrow \text{L}$  with 51 and 45% contributions, respectively [14]. An HOMO orbital is placed over an anthanthrene core and TPA unit, while an HOMO-3 orbital is located over an anthanthrene core and thiophene unit attached to a  $\text{TiO}_2$  cluster. LUMO orbitals are distributed on thiophene units and cyanoacrylic anchors. Now, we will discuss the distributions of HOMOs and LUMOs of the  $\text{D5@TiO}_2$  system as a representative example of the distribution in other designed dyes. The most important transitions in the  $\text{D5@TiO}_2$  system are from  $\text{H}-2 \rightarrow \text{L}$  to  $\text{H} \rightarrow \text{L}$  with 48 and 38% contributions, respectively. The  $\text{H}-2$  orbital is located over the whole skeleton of the D5 molecule except the two alkyl units and  $\text{TiO}_2$  cluster, while the HOMO orbital is distributed mainly on the TPA unit. In contrast, the LUMO orbital is delocalized on the thiophene unit attached to the  $\text{TiO}_2$  cluster.

With no exceptions, we can generalize the distribution of LUMO orbitals on the thiophene unit (acceptor unit) and cyanoacrylic acid (anchoring group) attached to the  $\text{TiO}_2$  cluster for all investigated dyes. On the other hand, for other LUMOs such as  $\text{L} + 3$ ,  $\text{L} + 4$ , and  $\text{L} + 15$ , the distribution is on the naphthacene core and thiophene unit of  $\text{TiO}_2$  in  $\text{D9@TiO}_2$  and mainly on the perylene core and pyrene cores in  $\text{D11@TiO}_2$  and  $\text{D8@TiO}_2$  clusters, respectively. Also, we can generalize that the major transitions in all investigated dyes involved a transition to LUMO orbitals. Also, we can say that the transitions occurred from the HOMO in most systems. Exceptions are  $\text{D8@TiO}_2$  and  $\text{D10@TiO}_2$ , where major transitions were not involved the HOMO orbital but in other orbitals such as  $\text{H}-2$  and  $\text{H}-3$ . In conclusion, in all adsorbed systems, comprehensible ICT from HOMO to LUMO orbitals was detected.

### 3.2.2. Maps of Molecular Electrostatic Potential and Electron Density Difference

The MESP of the adsorbed systems of dye@ $\text{TiO}_2$  are presented in Figure S6. The MESP of D2 and the designed dyes (D5 to D11) are quite similar, as in the case of the isolated dyes (see Section 4.2 in Additional Results and Discussion in SD). A key observation regarding the molecular electrostatic potential (MESP) of  $\text{D2@TiO}_2$  compared to the designed dyes is that D2 exhibits negative potentials from the  $\pi$ -linker core, along with the thiophene units. In contrast, the anchoring units (carboxylic group) and  $\text{TiO}_2$  clusters display positive potentials.

Conversely, in the designed dyes, the negative potential is localized primarily in the thiophene units, while the anchoring units and  $\text{TiO}_2$  clusters continue to exhibit positive potential. This observation may suggest a higher resonance energy of the anthanthrene core in D2 compared to the lower resonance energies associated with the cores of the designed dyes. Nevertheless, the distinct distribution of these electronic potentials facilitates charge separation, enabling efficient ICT from the dye to the  $\text{TiO}_2$  during the photoexcitation process. This, in turn, promotes effective charge injection. This conclusion can be confirmed by investigating the EDD maps of the adsorbed systems, see Figure 10, as follows. As we can notice, the EDD maps of the adsorbed systems show an accumulation of charge only on

the TiO<sub>2</sub> clusters. Therefore, during the photoexcitation from the ground to the first excited state, a complete CT occurs from the donor units through the  $\pi$ -linkers to the acceptor units, and finally, the total charge is delocalized on the TiO<sub>2</sub> clusters for all investigated systems.

### 3.2.3. Overall Performance of the Designed Dyes

Table 6 lists the most important properties (electronic and electrochemical parameters) of the designed dyes, along with those of the D2 dye, in correlation with their structural properties (core structures, resonance energies, and degree of planarity) to evaluate the overall performance of these designed dyes.

**Table 6.** Electronic and electrochemical parameters represented the overall performance of the designed isolated and adsorbed dyes in connection with their core structures, resonance energies, and degree of planarity.

Dye	Aromatic Core	E <sub>R</sub> (kJ/mol)	MPP	$\Delta_{L-H}$ (eV)	LHE (%)	− $\Delta G_{inj}$ (eV)	− $\Delta G_{reg}$ (eV)	$\lambda_{tot}$ (eV)	$\Delta\lambda$ (eV)	E <sub>ads</sub> (kJ/mol)
D2	Anthracene	694	2.042	4.030	97	0.50	1.45	0.607	0.296	−645.08
D5	Naphthalene	255	1.940	4.099	99	0.58	1.58	0.582	0.288	−660.16
D6	Anthracene	347	1.939	4.012	96	0.52	1.52	0.576	0.286	−655.58
D7	Phenanthrene	381	1.485	4.161	96	0.79	1.56	0.590	0.303	−653.67
D8	Pyrene	456	1.806	4.115	97	0.52	1.58	0.595	0.286	−653.47
D9	Naphthacene	460	1.962	3.863	95	0.76	1.44	0.579	0.286	−650.40
D10	Chrysene	487	0.914	4.174	95	0.72	1.57	0.592	0.291	−650.57
D11	Perylene	529	0.707	4.048	94	0.75	1.55	0.596	0.310	−647.63

In comparison with the D2 dye, the designed dyes D6 and D9, with lower E<sub>R</sub> values and a higher degree of planarity, show smaller  $\Delta_{L-H}$  values than the D2 dye, which means easier electron excitation and longer absorption wavelengths. All dyes harvest light efficiently within a range of 95–99%. In addition, the designed dyes (isolated and adsorbed) absorb light at longer wavelengths as their resonance energies of the aromatic rings increase. Obtaining the optimal values and negative values of  $\Delta G_{reg}$  ( $\geq 0.4$  eV) and  $\Delta G_{inj}$  ( $\gg 0.2$  eV), the designed dyes have greater  $\Delta G_{inj}$  and  $\Delta G_{reg}$  (except D9) values than that of the D2 dye molecule. This implies that the new design of dyes improves the processes of dye regeneration and electron injection.

The designed dyes show a favorable electron–hole transport (except D7 and D11) and the total reorganization energy, and thus, recombination processes are rendered. Finally, all dyes bind chemically to the TiO<sub>2</sub> cluster, and the designed dyes show stronger adsorption with a red/blue shift in their light absorbance, indicating an aggregation of the dye molecules at the TiO<sub>2</sub> surface. Notably, D9, with a naphthacene core and moderate E<sub>R</sub> (=460 kJ/mol), displayed balanced hole and electron hopping mobilities and a reduced energy gap, leading to excellent charge-transfer properties.

## 4. Conclusions

This study examines the impact of cores with varying resonance energies on the properties of anthanthrene-based dyes, utilizing DFT methods. An experimental validation of the computational approach was achieved through testing one of the dyes (D2) in a DSSC, which yielded good performance. The following conclusions were reached:



- Although the designed dyes exhibit similar properties to D2 in energy-level alignment and molecular electrostatic potentials (MESP), D2 outperformed the others by its higher HOMO energy.
- D6 and D9, with lower resonance energies and greater planarity than D2, show smaller energy gaps, facilitating easier electron excitation and longer wavelength absorption.
- All designed dyes demonstrate high LHEs (95–99%).
- The designed dyes (isolated and adsorbed) absorb light at longer wavelengths due to increased resonance energies of the aromatic rings, with most exhibiting greater  $\Delta G_{inj}$  and  $\Delta G_{reg}$  values compared to D2, suggesting enhanced dye regeneration and electron injection processes.
- Most of the designed dyes demonstrate favorable electron–hole transport properties, reducing reorganization energy and mitigating recombination.
- All dyes bind chemically to the  $TiO_2$  cluster, with the designed dyes showing stronger adsorption and red/blue shifts in absorbance spectra.
- D9, with a naphthacene core, shows moderate resonance energy, achieving balanced mobilities and reduced energy gaps for excellent charge-transfer characteristics.

Notably, the relationship between ICT and resonance energy is not straightforward, though the results highlight the importance of aromaticity in optimizing photovoltaic performance. In conclusion, the newly designed dyes exhibit enhanced electronic and electrochemical properties, making them promising candidates for use as photosensitizers in dye-sensitized solar cells, with implications for optimizing aromatic bridges in molecular photovoltaic applications.

**Supplementary Materials:** The following supporting information can be downloaded at: <https://www.mdpi.com/article/10.3390/pr13020418/s1>, Figure S1: Energy levels of FMOs of the  $\pi$ -cores of D2, and D5 to D11 dyes; Figure S2: Left: NCI-RDG 2D scatter maps, and right: 3D colour-filled RDG isosurfaces of investigated dye dimers at CPCM/M06-2x/6-31+G(d,p) in THF; Figure S3: Total density of states (TDOS) plots of the adsorbed systems of dye@ $TiO_2$ ; Figure S4: Simulated absorption spectra of dye@ $TiO_2$  systems in THF; Figure S5: MESP of the eight investigated dyes in their isolated and adsorbed (on  $TiO_2$ ) forms at iso-value 0.1 au; Figure S6: ELF of dye molecules before and after adsorption on  $TiO_2$ ; Figure S7: Dipole moments ( $\mu_{GS}$ ,  $\mu_{ES}$  and  $\Delta\mu$ ) (in Debye) of D2, and D5 to D11 dyes; Figure S8: LHE and  $\eta$  relationship of D2, and D5 to D11 dyes; Table S1: Hole, electron, hole-electron, and total reorganization energies ( $\lambda_{hole}$ ,  $\lambda_{elec}$ ,  $\Delta\lambda$  and  $\lambda_{tot}$ , respectively); Table S2: Le Bahers's CT indices included the charge transfer distance D, H, t (in Å), and the amount of charge transferred q (in e) of the seven designed dyes along with those of D2 dye calculated at the CPCM/TDCAM-B3LYP/6-31+G(d,p) in THF. Note: data for D10 dye not converged and not included; Table S3: GSEO, ESOPs, EDye and EDye\*, excitation energy  $E_{ex}$ , and free energies of charge injection and dye regeneration,  $\Delta G_{inj}$ ,  $\Delta G_{reg}$ , respectively, (in eV) of the isolated dyes calculated at CPCM/TDCAM-B3LYP/6-31G(d,p) in THF; Table S4: Adsorption energies (in kJ/mol) and their energy components (in Hartree) of the eight dye@ $TiO_2$  adsorbed systems. Note: data of D2 dye are collected from ref. [17]; Table S5: Ti–O bond lengths of the dye@ $TiO_2$  adsorbed systems calculated at CPCM/M06-2x with 6-31+G(d,p) and LANL2DZ in THF; Table S6: Energies of HOMOs, LUMOs of isolated and adsorbed dyes, CB, and VB of  $TiO_2$ , and their dipole moments (in Debye) calculated at CPCM/M06-2x with 6-31+G(d,p) and LANL2DZ in THF; Table S7: Ground state, excited state, and change dipole moments ( $\mu_{GS}$ ,  $\mu_{ES}$ , and  $\Delta\mu$ , respectively) in Debye; Table S8: Computed molecular parameters of the eight investigated dyes.

**Funding:** This project was funded by a KAU Endowment (WAQF) at King Abdulaziz University, Jeddah, under grant number (WAQF: 122-247-2024). The author, therefore, acknowledges, with thanks, WAQF and the Deanship of Scientific Research (DSR) for technical and financial support. The author acknowledges King Abdulaziz University's High-Performance Computing Centre (Aziz

Supercomputer) (<http://hpc.kau.edu.sa>) for supporting the computation of the work described in this paper.

**Data Availability Statement:** The original contributions presented in this study are included in the article/Supplementary Material. Further inquiries can be directed to the corresponding author.

**Conflicts of Interest:** The author declares no conflict of interest.

## References

1. Tyagi, H.; Chakraborty, P.R.; Powar, S.; Agarwal, A.K. (Eds.) *Solar Energy: Systems, Challenges, and Opportunities*, 1st ed.; Springer: Berlin/Heidelberg, Germany, 2020; p. 423.
2. Archer, D. *Global Warming: Understanding the Forecast*; John Wiley & Sons: Hoboken, NJ, USA, 2012.
3. O'Regan, B.; Grätzel, M. A low-cost, high-efficiency solar cell based on dye-sensitized colloidal TiO<sub>2</sub> films. *Nature* **1991**, *353*, 737–740. [[CrossRef](#)]
4. Muñoz-García, A.B.; Benesperi, I.; Boschloo, G.; Concepcion, J.J.; Delcamp, J.H.; Gibson, E.A.; Meyer, G.J.; Pavone, M.; Pettersson, H.; Hagfeldt, A.; et al. Dye-sensitized solar cells strike back. *Chem. Soc. Rev.* **2021**, *50*, 12450–12550. [[CrossRef](#)]
5. Borges-Martínez, M.; Alvarez, D.; Montenegro-Pohlhammer, N.; Menéndez, M.I.; López, R.; Cárdenas-Jirón, G. Assessment of BODIPY–Oxasmaragdyrin Dyads for Dye-Sensitized Solar Cells: Aromaticity, Photosensitization Capability, and Charge Transport. *J. Phys. Chem. C* **2019**, *123*, 19362–19375. [[CrossRef](#)]
6. He, J.; Wang, B.; Chang, S.; Chen, T. Ruthenium-Based Photosensitizers for Dye-Sensitized Solar Cells. In *Organometallics and Related Molecules for Energy Conversion*; Wong, W.-Y., Ed.; Springer: Berlin/Heidelberg, Germany, 2015; pp. 91–114.
7. Aksakal, N.E.; Kazan, H.H.; Eçik, E.T.; Yuksel, F. A novel photosensitizer based on a ruthenium(ii) phenanthroline bis(perylenediimide) dyad: Synthesis, generation of singlet oxygen and in vitro photodynamic therapy. *New J. Chem.* **2018**, *42*, 17538–17545. [[CrossRef](#)]
8. Al Mogren, M.M.; Ahmed, N.M.; Hasanein, A.A. Molecular modeling and photovoltaic applications of porphyrin-based dyes: A review. *J. Saudi Chem. Soc.* **2020**, *24*, 303–320. [[CrossRef](#)]
9. Obasuyi, A.R.; Glossman-Mitnik, D.; Flores-Holguín, N. Electron injection in anthocyanidin and betalain dyes for dye-sensitized solar cells: A DFT approach. *J. Comput. Electron.* **2019**, *18*, 396–406. [[CrossRef](#)]
10. Dhar, A.; Kumar, N.S.; Paul, P.K.; Roy, S.; Vekariya, R.L. Influence of tagging thiophene bridge unit on optical and electrochemical properties of coumarin based dyes for DSSCs with theoretical insight. *Org. Electron.* **2018**, *53*, 280–286. [[CrossRef](#)]
11. Ayare, N.N.; Sharma, S.; Sonigara, K.K.; Prasad, J.; Soni, S.S.; Sekar, N. Synthesis and computational study of coumarin thiophene-based D- $\pi$ -A azo bridge colorants for DSSC and NLOphoric application. *J. Photochem. Photobiol. A Chem.* **2020**, *394*, 112466. [[CrossRef](#)]
12. Pounraj, P.; Mohankumar, V.; Pandian, M.S.; Ramasamy, P. The effect of different  $\pi$ -bridge configuration on bi-anchored triphenylamine and phenyl modified triphenylamine based dyes for dye sensitized solar cell (DSSC) application: A theoretical approach. *J. Mol. Graph. Model.* **2018**, *79*, 235–253. [[CrossRef](#)]
13. Al-Temime, F.; Mraity, H. DFT/TD-DFT investigation of novel D- $\pi$ -A configuration dyes for improving solar cell efficiency. *Struct. Chem.* **2022**, *33*, 859–869. [[CrossRef](#)]
14. Wazzan, N. Theoretical investigation of anthanthrene-based dyes in dye-sensitized solar cell applications: Effect of nature of alkyl-substitutions and number of anchoring groups. *Arab. J. Chem.* **2022**, *15*, 103969. [[CrossRef](#)]
15. Geng, Y.; Yi, C.; Bircher, M.P.; Decurtins, S.; Cascella, M.; Grätzel, M.; Liu, S.-X. Anthanthrene dye-sensitized solar cells: Influence of the number of anchoring groups and substitution motif. *RSC Adv.* **2015**, *5*, 98643–98652. [[CrossRef](#)]
16. Giguère, J.-B.; Verolet, Q.; Morin, J.-F. 4,10-Dibromoanthanthrone as a New Building Block for p-Type, n-Type, and Ambipolar  $\pi$ -Conjugated Materials. *Chem.—A Eur. J.* **2013**, *19*, 372–381. [[CrossRef](#)]
17. Venkatraman, R.; Panneer, S.V.K.; Varathan, E.; Subramanian, V. Aromaticity–Photovoltaic Property Relationship of Triphenylamine-Based D- $\pi$ -A Dyes: Leads from DFT Calculations. *J. Phys. Chem. A* **2020**, *124*, 3374–3385. [[CrossRef](#)] [[PubMed](#)]
18. Pino-Rios, R.; Montenegro-Pohlhammer, N.; Cárdenas-Jirón, G. Assessment of New Expanded Porpholactones as UV/Vis/NIR Chromophores for Dye-Sensitized Solar Cell Applications. *J. Phys. Chem. A* **2021**, *125*, 2267–2275. [[CrossRef](#)]
19. Silva López, C.; Nieto Faza, O. 2—Overview of the computational methods to assess aromaticity. In *Aromaticity*; Fernandez, I., Ed.; Elsevier: Amsterdam, The Netherlands, 2021; pp. 41–71.
20. Prajapat, K.; Dhonde, M.; Sahu, K.; Bhojane, P.; Murty, V.V.S.; Shirage, P.M. The evolution of organic materials for efficient dye-sensitized solar cells. *J. Photochem. Photobiol. C Photochem. Rev.* **2023**, *55*, 100586. [[CrossRef](#)]

21. Zhao, Y.; Truhlar, D.G. The M06 suite of density functionals for main group thermochemistry, thermochemical kinetics, noncovalent interactions, excited states, and transition elements: Two new functionals and systematic testing of four M06-class functionals and 12 other functionals. *Theor. Chem. Acc.* **2008**, *120*, 215–241. [[CrossRef](#)]
22. Ditchfield, R.; Hehre, W.J.; Pople, J.A. Self-Consistent Molecular-Orbital Methods. IX. An Extended Gaussian-Type Basis for Molecular-Orbital Studies of Organic Molecules. *J. Chem. Phys.* **1971**, *54*, 724–728. [[CrossRef](#)]
23. Clark, T.; Chandrasekhar, J.; Spitznagel, G.W.; Schleyer, P.V.R. Efficient diffuse function-augmented basis sets for anion calculations. III. The 3-21+G basis set for first-row elements, Li–F. *J. Comput. Chem.* **1983**, *4*, 294–301. [[CrossRef](#)]
24. Josa, D.; Rodríguez-Otero, J.; Cabaleiro-Lago, E.M.; Rellán-Piñeiro, M. Analysis of the performance of DFT-D, M05-2X and M06-2X functionals for studying  $\pi \cdots \pi$  interactions. *Chem. Phys. Lett.* **2013**, *557*, 170–175. [[CrossRef](#)]
25. Walker, M.; Harvey, A.J.A.; Sen, A.; Dessent, C.E.H. Performance of M06, M06-2X, and M06-HF Density Functionals for Conformationally Flexible Anionic Clusters: M06 Functionals Perform Better than B3LYP for a Model System with Dispersion and Ionic Hydrogen-Bonding Interactions. *J. Phys. Chem. A* **2013**, *117*, 12590–12600. [[CrossRef](#)]
26. Delgado-Montiel, T.; Soto-Rojas, R.; Baldenebro-López, J.; Glossman-Mitnik, D. Theoretical Study of the Effect of Different  $\pi$  Bridges Including an Azomethine Group in Triphenylamine-Based Dye for Dye-Sensitized Solar Cells. *Molecules* **2019**, *24*, 3897. [[CrossRef](#)] [[PubMed](#)]
27. Wu, W.; Li, Y.; Zhang, J.; Guo, X.; Wang, L.; Ågren, H. Theoretical modelling of metal-based and metal-free dye sensitizers for efficient dye-sensitized solar cells: A review. *Sol. Energy* **2024**, *277*, 112748. [[CrossRef](#)]
28. Barone, V.; Cossi, M. Quantum Calculation of Molecular Energies and Energy Gradients in Solution by a Conductor Solvent Model. *J. Phys. Chem. A* **1998**, *102*, 1995–2001. [[CrossRef](#)]
29. Cossi, M.; Rega, N.; Scalmani, G.; Barone, V. Energies, structures, and electronic properties of molecules in solution with the C-PCM solvation model. *J. Comput. Chem.* **2003**, *24*, 669–681. [[CrossRef](#)]
30. Wazzan, N.; Irfan, A. Theoretical study of triphenylamine-based organic dyes with mono-, di-, and tri-anchoring groups for dye-sensitized solar cells. *Org. Electron.* **2018**, *63*, 328–342. [[CrossRef](#)]
31. Syzgantseva, O.A.; Gonzalez-Navarrete, P.; Calatayud, M.; Bromley, S.; Minot, C. Theoretical Investigation of the Hydrogenation of (TiO<sub>2</sub>)<sub>N</sub> Clusters (N = 1–10). *J. Phys. Chem. C* **2011**, *115*, 15890–15899. [[CrossRef](#)]
32. Hay, P.J.; Wadt, W.R. Ab initio effective core potentials for molecular calculations. Potentials for the transition metal atoms Sc to Hg. *J. Chem. Phys.* **1985**, *82*, 270–283. [[CrossRef](#)]
33. Yanai, T.; Tew, D.P.; Handy, N.C. A new hybrid exchange–correlation functional using the Coulomb-attenuating method (CAM-B3LYP). *Chem. Phys. Lett.* **2004**, *393*, 51–57. [[CrossRef](#)]
34. Frisch, M.J. *Gaussian 09 Programmer's Reference*; Gaussian: Wallingford, England, 2009.
35. Dennington, R.; Keith, T.; Millam, J. *GaussView*; Version 5; Semichem Inc.: Shawnee, KS, USA, 2009.
36. Hanwell, M.D.; Curtis, D.E.; Lonie, D.C.; Vandermeersch, T.; Zurek, E.; Hutchison, G.R. Avogadro: An advanced semantic chemical editor, visualization, and analysis platform. *J. Cheminformatics* **2012**, *4*, 17. [[CrossRef](#)]
37. Deogratias, G.; Al-Qurashi, O.S.; Wazzan, N.; Pogrebnya, T.; Pogrebnoi, A. Effects of heteroatoms in  $\pi$ -conjugated linkers on the optical and electronic properties of modified triphenylamine based dyes: Towards DSSCs' applications. *J. Mol. Model.* **2020**, *26*, 288. [[CrossRef](#)] [[PubMed](#)]
38. Lu, T. Simple, reliable, and universal metrics of molecular planarity. *J. Mol. Model.* **2021**, *27*, 263. [[CrossRef](#)] [[PubMed](#)]
39. Lu, T.; Chen, F. Multiwfn: A multifunctional wavefunction analyzer. *J. Comput. Chem.* **2012**, *33*, 580–592. [[CrossRef](#)] [[PubMed](#)]
40. Zhang, G.; Bai, Y.; Li, R.; Shi, D.; Wenger, S.; Zakeeruddin, S.M.; Grätzel, M.; Wang, P. Employ a bithienothiophene linker to construct an organic chromophore for efficient and stable dye-sensitized solar cells. *Energy Environ. Sci.* **2009**, *2*, 92–95. [[CrossRef](#)]
41. Cahen, D.; Hodes, G.; Grätzel, M.; Guillemoles, J.F.; Riess, I. Nature of Photovoltaic Action in Dye-Sensitized Solar Cells. *J. Phys. Chem. B* **2000**, *104*, 2053–2059. [[CrossRef](#)]
42. Som, N.N.; Sampath, P.M.W.P.; Dabhi, S.D.; Mankad, V.; Shinde, S.; Attygalle, M.L.C.; Jha, P.K. Strain and layer modulated electronic and optical properties of low dimensional perovskite methylammonium lead iodide: Implications to solar cells. *Sol. Energy* **2018**, *173*, 1315–1322. [[CrossRef](#)]
43. Martinsovich, N.; Troisi, A. Theoretical studies of dye-sensitized solar cells: From electronic structure to elementary processes. *Energy Environ. Sci.* **2011**, *4*, 4473–4495. [[CrossRef](#)]
44. Lin, J.T.; Chen, P.-C.; Yen, Y.-S.; Hsu, Y.-C.; Chou, H.-H.; Yeh, M.-C.P. Organic Dyes Containing Furan Moiety for High-Performance Dye-Sensitized Solar Cells. *Org. Lett.* **2009**, *11*, 97–100. [[CrossRef](#)]
45. Bora, S.R.; Kalita, D.J. Tuning the charge transfer and optoelectronic properties of tetrathiafulvalene based organic dye-sensitized solar cells: A theoretical approach. *RSC Adv.* **2021**, *11*, 39246–39261. [[CrossRef](#)]
46. Hilborn, R.C. Einstein coefficients, cross sections, f values, dipole moments, and all that. *Am. J. Phys.* **1982**, *50*, 982–986. [[CrossRef](#)]
47. Marcus, R.A. Electron transfer reactions in chemistry. Theory and experiment. *Rev. Mod. Phys.* **1993**, *65*, 599–610. [[CrossRef](#)]

48. Wazzan, N.A. A DFT/TDDFT investigation on the efficiency of novel dyes with ortho-fluorophenyl units (A1) and incorporating benzotriazole/benzothiadiazole/phthalimide units (A2) as organic photosensitizers with D–A2– $\pi$ –A1 configuration for solar cell applications. *J. Comput. Electron.* **2019**, *18*, 375–395. [\[CrossRef\]](#)
49. Marcus, R.A. Chemical and Electrochemical Electron-Transfer Theory. *Annu. Rev. Phys. Chem.* **1964**, *15*, 155–196. [\[CrossRef\]](#)
50. Chen, Z.; Li, Y.; He, Z.; Xu, Y.; Yu, W. Theoretical investigations on charge transport properties of tetrabenzo[a,d,j,m]coronene derivatives using different density functional theory functionals (B3LYP, M06-2X, and wB97XD). *J. Chem. Res.* **2019**, *43*, 293–303. [\[CrossRef\]](#)
51. Wazzan, N.; El-Shishtawy, R.M.; Irfan, A. DFT and TD-DFT calculations of the electronic structures and photophysical properties of newly designed pyrene-core arylamine derivatives as hole-transporting materials for perovskite solar cells. *Theor. Chem. Acc.* **2017**, *137*, 9. [\[CrossRef\]](#)
52. Alongamo, C.I.L.; Tasheh, S.N.; Nkungli, N.K.; Bine, F.K.; Ghogomu, J.N. Structural, Electronic, and Charge Transport Properties of New Materials based on 2-(5-Mercapto-1,3,4-Oxadiazol-2-yl) Phenol for Organic Solar Cells and Light Emitting Diodes by DFT and TD-DFT. *J. Chem.* **2022**, *2022*, 1802826. [\[CrossRef\]](#)
53. Johnson, E.R.; Keinan, S.; Mori-Sánchez, P.; Contreras-García, J.; Cohen, A.J.; Yang, W. Revealing Noncovalent Interactions. *J. Am. Chem. Soc.* **2010**, *132*, 6498–6506. [\[CrossRef\]](#)
54. Le Bahers, T.; Adamo, C.; Ciofini, I. A Qualitative Index of Spatial Extent in Charge-Transfer Excitations. *J. Chem. Theory Comput.* **2011**, *7*, 2498–2506. [\[CrossRef\]](#)
55. Ali, B.A.; Allam, N.K. Propping the optical and electronic properties of potential photo-sensitizers with different  $\pi$ -spacers: TD-DFT insights. *Spectrochim. Acta Part A Mol. Biomol. Spectrosc.* **2018**, *188*, 237–243. [\[CrossRef\]](#)
56. Li, P.; Cui, Y.; Song, C.; Zhang, H. A systematic study of phenoxazine-based organic sensitizers for solar cells. *Dye. Pigm.* **2017**, *137*, 12–23. [\[CrossRef\]](#)
57. Wu, H.; Zhang, T.; Wu, C.; Guan, W.; Yan, L.; Su, Z. A theoretical design and investigation on Zn-porphyrin-polyoxometalate hybrids with different  $\pi$ -linkers for searching high performance sensitizers of p-type dye-sensitized solar cells. *Dye. Pigm.* **2016**, *130*, 168–175. [\[CrossRef\]](#)
58. Wei, S.; Li, K.; Lu, X.; Zhao, Z.; Shao, Y.; Dang, Y.; Li, S.; Guo, W. Theoretical insight into electronic structure and optoelectronic properties of heteroleptic Cu(I)-based complexes for dye-sensitized solar cells. *Mater. Chem. Phys.* **2016**, *173*, 139–145. [\[CrossRef\]](#)
59. Zanjanchi, F.; Beheshtian, J. Natural pigments in dye-sensitized solar cell (DSSC): A DFT-TDDFT study. *J. Iran. Chem. Soc.* **2019**, *16*, 795–805. [\[CrossRef\]](#)
60. Li, Y.; Zhang, W.; Li, X.; Xu, Y. Boosting the photoelectric conversion efficiency of DSSCs through graphene quantum dots: Insights from theoretical study. *Mater. Chem. Front.* **2021**, *5*, 5814–5825. [\[CrossRef\]](#)
61. Al-Qurashi, O.S.; Wazzan, N.A.; Obot, I. Exploring the effect of mono- and di-fluorinated triphenylamine-based molecules as electron donors for dye-sensitized solar cells. *Mol. Simul.* **2020**, *46*, 41–53. [\[CrossRef\]](#)
62. Costa, R.; Al-Qurashi, O.S.; Wazzan, N.; Pogrebnoi, A.; Pogrebnya, T. Designed complexes based on betanidin and L0 Dyes for DSSCs: Thermodynamic and optoelectronic properties from DFT study. *Mol. Simul.* **2022**, *48*, 647–661. [\[CrossRef\]](#)
63. Irfan, A.; Chaudhry, A.R.; Jin, R.; Al-Sehemi, A.G.; Muhammad, S.; Tang, S. Exploring the charge transfer nature and electro-optical properties of anthracene based sensitizers @TiO<sub>2</sub> cluster. *J. Taiwan Inst. Chem. Eng.* **2017**, *80*, 239–246. [\[CrossRef\]](#)
64. Soria, F.A.; Daldossi, C.; Di Valentin, C. Tuning the electron injection mechanism by changing the adsorption mode: The case study of Alizarin on TiO<sub>2</sub>. *Mater. Today Energy* **2022**, *28*, 101085. [\[CrossRef\]](#)
65. Britel, O.; Fitri, A.; Touimi Benjelloun, A.; Slimi, A.; Benzakour, M.; McHarfi, M. Theoretical design of new carbazole based organic dyes for DSSCs applications. A DFT/TD-DFT insight. *J. Photochem. Photobiol. A Chem.* **2022**, *429*, 113902. [\[CrossRef\]](#)
66. Horn, M.; Schwerdtfeger, C.F.; Meagher, E.P. Refinement of the structure of anatase at several temperatures. *Z. Für Krist.* **1972**, *136*, 273. [\[CrossRef\]](#)
67. Bates, S.P.; Kresse, G.; Gillan, M.J. The adsorption and dissociation of ROH molecules on TiO<sub>2</sub>(110). *Surf. Sci.* **1998**, *409*, 336–349. [\[CrossRef\]](#)
68. Al-Qurashi, O.S.; Wazzan, N. Prediction of Power Conversion Efficiencies of Diphenylthienylamine-Based Dyes Adsorbed on the Titanium Dioxide Nanotube. *ACS Omega* **2021**, *6*, 8967–8975. [\[CrossRef\]](#) [\[PubMed\]](#)
69. Dette, C.; Pérez-Osorio, M.A.; Kley, C.S.; Punke, P.; Patrick, C.E.; Jacobson, P.; Giustino, F.; Jung, S.J.; Kern, K. TiO<sub>2</sub> anatase with a bandgap in the visible region. *Nano Lett.* **2014**, *14*, 6533–6538. [\[CrossRef\]](#)
70. Jin, X.; Sun, L.; Li, D.; Wang, C.-L.; Bai, F.-Q. Efficiency difference between furan- and thiophene-based D– $\pi$ –A dyes in DSSCs explained by theoretical calculations. *RSC Adv.* **2018**, *8*, 29917–29923. [\[CrossRef\]](#) [\[PubMed\]](#)
71. Dualeh, A.; Angelis, F.; Fantacci, S.; Moehl, T.; Yi, C.; Kessler, F.; Baranoff, E.; Nazeeruddin, M.; Graetzel, M. Influence of Donor Groups of Organic D– $\pi$ –A Dyes on Open-Circuit Voltage in Solid-State Dye-Sensitized Solar Cells. *J. Phys. Chem. C* **2012**, *116*, 1572–1578. [\[CrossRef\]](#)

72. Heng, P.; Mao, L.; Guo, X.; Wang, L.; Zhang, J. Accurate estimation of the photoelectric conversion efficiency of a series of anthracene-based organic dyes for dye-sensitized solar cells. *J. Mater. Chem. C* **2020**, *8*, 2388–2399. [[CrossRef](#)]
73. He, L.-J.; Chen, J.; Bai, F.-Q.; Jia, R.; Wang, J.; Zhang, H.-X. Fine-tuning  $\pi$ -spacer for high efficiency performance DSSC: A theoretical exploration with D– $\pi$ –A based organic dye. *Dye. Pigment.* **2017**, *141*, 251–261. [[CrossRef](#)]

**Disclaimer/Publisher’s Note:** The statements, opinions and data contained in all publications are solely those of the individual author(s) and contributor(s) and not of MDPI and/or the editor(s). MDPI and/or the editor(s) disclaim responsibility for any injury to people or property resulting from any ideas, methods, instructions or products referred to in the content.